Dynamic responses in shocked Cu-Zr nanoglasses with gradient microstructure

Yunlong Guan [a], Weidong Song [a,*], Yunjiang Wang [b], Shanshan Liu [a], Yongji Yu [a]

[a] State Key Laboratory of Explosion Science and Technology, Beijing Institute of Technology, Beijing, 100081, China
[b] State Key Laboratory of Nonlinear Mechanics, Institute of Mechanics, Chinese Academy of Sciences (CAS), Beijing 100190, China

ARTICLE INFO

ABSTRACT

Shock is one of the physical processes that materials are most likely to suffer during applications, therefore the elusive shock properties of nanoglasses are unacceptable. Additionally, establishing gradient microstructure is a promising approach to optimize mechanics properties further. Here, shock characteristics of $Cu_{64}Zr_{36}$ nanoglasses with gradient microstructures are systematically investigated by molecular dynamics simulations in the particle velocity range of 0.5 to 5 km/s. Two types of gradient nanoglasses (GNGs) along the shock direction are prepared and analyzed, i. e., a negative gradient structure (S1) in contrast with a positive gradient structure (S2). The results show that the number of mechanically stable $<0,0,12,0>$ and $<0,1,10,2>$ atomic Voronoi polyhedra, which are typical building blocks of the amorphous structure in terms of Voronoi tessellation method, in grain interfaces is significantly less than that in grain interiors. As a result, the local free volume gradually changes along the shock direction by the designed gradient structure, which causes a significant impact on the shock wave profiles of shear strain, stress, configurational entropy, and temperature in the GNGs. However, due to a similar chemically-disordered feature in grain interiors and interfaces, the shock wave speeds of nanoglasses are not sensitive to grain sizes under the same shock strength, contrary to the usual shock wave speed mechanism in conventional polycrystalline. Thus, unlike traditional polycrystalline with grain size gradient, the indirect free-surface method of estimating spall strength is still applicable to the GNGs. Finally, the positive gradient structure results in lower temperature and free volume in the spall region, which causes the spall strengths of the S2 sample higher than those of the S1 sample.

1. Introduction

Metallic glass (MG) was a new class of metal materials due to its unique atomic configuration. Some unique properties, differing from the crystalline counterparts, have been found in MGs because they lack atomic periodicity in the long-range and exhibit chemical short-range atomic order(Greer et al., 2013; Schuh et al., 2007). In 1960, Klement et al.(Klement et al., 1960) first prepared an MG sample by quenching a molten $Au_{80}Si_{20}$ alloy with an extremely high cooling rate of 10^6 K/s. Unlike crystalline materials, there are no crystal defects (e.g., grain boundaries and dislocations, etc.) in MGs, so they possess excellent mechanical properties, such as high strength, hardness, elastic limit, and elastic energy storage(Donovan and Stobbs, 1981; Gan et al., 2019; Kosiba et al., 2019; Polk and Turnbull, 1972; Sha et al., 2017; Wang et al., 2011; Wu et al., 2011). Therefore, MGs are considered an ideal candidate material in

---

defense, aviation, and aerospace, and so far, received intense investigation(Chen et al., 2011; Guan et al., 2021; Shan et al., 2008; Sharma et al., 2009).

Unfortunately, MGs have not yet been widely applied because of their low ductility at room temperature. Recently, the results of theoretical, numerical, and experimental studies have shown that this low ductility is essentially caused by their compositions and processing technologies, which generate their unique atom configuration(Cheng et al., 2008a; Lewandowski, 2001; Şopu et al., 2011; Tang et al., 2021). For a given atomic composition, the mechanical properties of MGs can be altered significantly by changing element ratio or adjusting processing methods (e.g., adopting different annealing times or quenching rates)(Narayan et al., 2014; Ramamurty
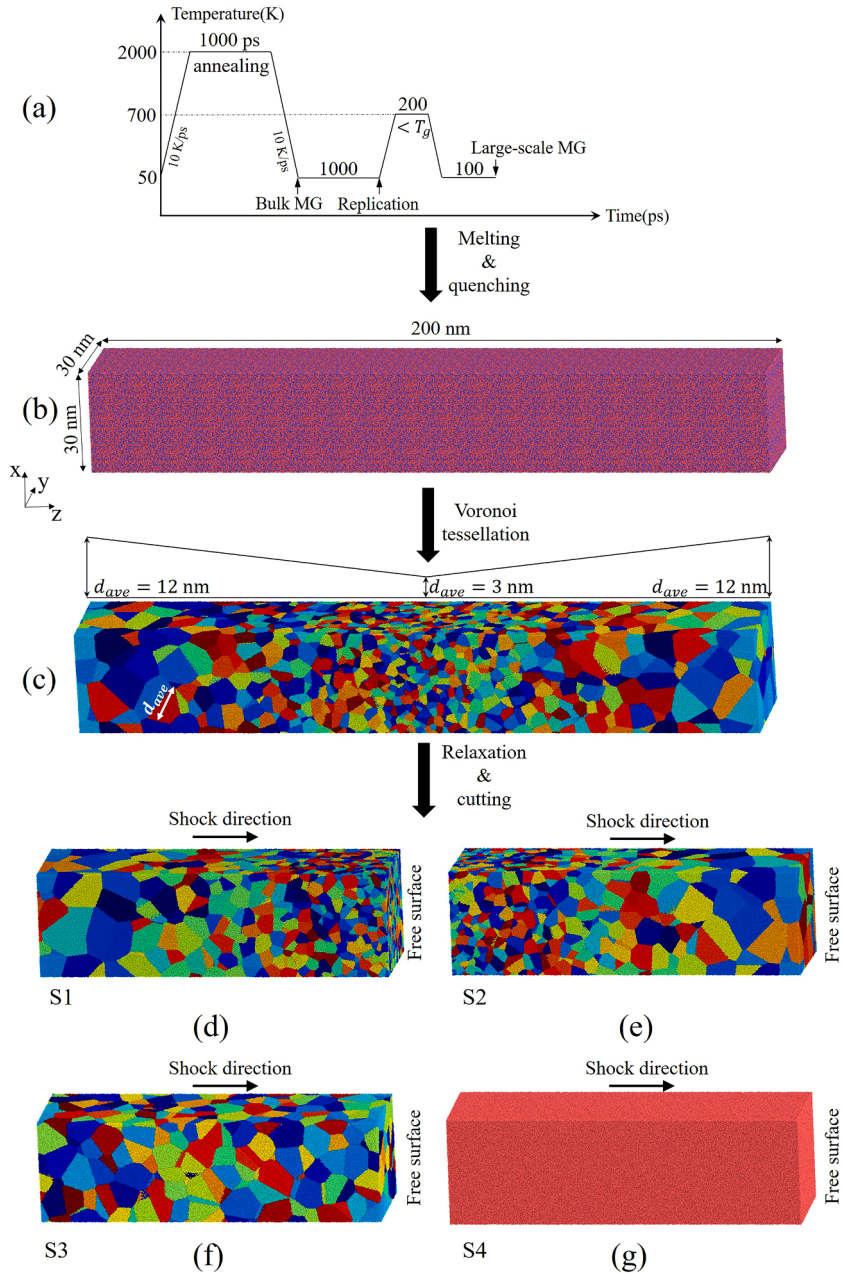

Fig. 1. (a) Schematic for generating the large-scale $Cu_{64}Zr_{36}$ MG by melting/quenching procedure. (b) Displaying the size information (30 nm ×30 nm ×200 nm) of the large-scale $Cu_{64}Zr_{36}$ MG. (c) The establishment of initial nanoglass with linear gradient structure by using the Poisson-Voronoi tessellation. Then, two gradient nanoglasses (GNGs) are obtained by cutting the initial nanoglass. (d) A negative gradient sample (S1) with decreasing grain sizes along the shock direction. (e) A positive gradient sample (S2) with increasing grain sizes along the shock direction. As a comparison, we also created two homogeneous samples. (f) Homogeneous nanoglass with grain size of 8 nm (S3). (g) Homogeneous $Cu_{64}Zr_{36}$ MG (S4).

et al., 2002; Shi and Falk, 2006; Winkler et al., 2008). According to Mauro et al.'s speculation(Mauro et al., 2011), the altered properties may be derived from the changes in atomic structure topology, i.e., the statistics of the number and structure of Voronoi polyhedra. E.g., the perfect icosahedron (<0,0,12,0> cluster) in the Cu-rich CuZr MGs has been certificated as a key microstructural feature(Mauro et al., 2011). The fraction of this cluster controls the elastic limit and yield strength, and determines the shear deformation behavior(Cheng et al., 2009; Wang et al., 2008). Therefore, an appropriate change in the statistics of atomic Voronoi polyhedral clusters by the element ratio and processing technology can improve ductility. However, the improvement is still limited.

To further improve MGs' ductility, researchers propose many strategies, such as nanoporous MGs(Inoue et al., 2007; Luo et al., 2018; Wada et al., 2005; Zhao et al., 2013), multiphase MGs(Chen et al., 2020; He et al., 2003; Pauly et al., 2010), and nanoglasses (Adibi et al., 2014; Ritter et al., 2011). At present, nanoglasses have been proposed as a new type of MG materials. In terms of the preparation, nanoglasses are synthesized by cold compaction of metallic glass particles that were generated by inert gas condensation (Adjaoud and Albe, 2016, 2018; Fang et al., 2012; Ritter et al., 2011; Wang et al., 2017; Weissmüller et al., 1992). The microstructure of nanoglasses comprises bulk glassy regions (grain interiors) and grain interfaces, which constitutes a distinct structure different from bulk MGs. Preliminary modeling studies of nanoglasses have shown considerable ductility improvement compared with conventional MGs counterparts(Adibi et al., 2014; Albe et al., 2013). According to molecular dynamics (MD) simulations, Adibi et al.(Adibi et al., 2014) found a homogeneous superplastic flow in a nanoglass under tensile loading when the grain size was small. The homogeneous superplastic behaviors are caused by the existence of grain interfaces that increase with decreasing grain size and are the preferred channels of plastic deformation, thereby significantly enhancing the overall ductility of nanoglasses. For conventional MGs, a single dominant shear band is formed at localization resulting in catastrophic failure. Although these preliminary explorations of nanoglasses have shown encouraging ductility, their strengths reduced at the expense. Therefore, to couple strength and ductility, there has been a strong interest in the investigations of composite structures(Qiu et al., 2021), e.g., Sha et al.(Sha et al., 2015) proposed a bimodal grain size nanoglass, and Albe et al.(Albe et al., 2013) designed the dual-phase nanoglasses. These composite nanoglasses did obtain some compromise between strength and ductility. Most recently, Yuan et al.(Yuan and Branicio, 2020) established three types of gradient nanoglasses (GNGs) with the seamless linear distribution of grain sizes and performed tensile loading on these GNGs. They found that the gradient microstructure induces shear band constraint, delocalization, and delayed failure, thereby synergizes strength and ductility in nanoglasses. These pioneering investigations, all aimed at the preparation process and improving mechanical properties, significantly impacted nanoglasses. As a material expected to be used in extreme environments, such as aviation and aerospace, the investigation on shock behavior of nanoglasses are urgent and critical. Regrettably, the shock characteristics and spallation of nanoglasses remain elusive for both the experiments and simulations. Additionally, the effect of gradient microstructure on the shock characteristics of nanoglasses is also unknown.

Generally, the utilization of gradient structure is one of the crucial means to tune material characteristics(Islam et al., 2020; Wei and Xu, 2021). In this work, the shock pulses are employed to study the effects of gradient microstructure on the shear deformation behavior, shock stress, temperature, shock wave velocity, spall fracture behavior, and spall strength in a $Cu_{64}Zr_{36}$ nanoglass under MD simulations. Consolidating glassy grains in the size range of 3 to 12 nm, there mainly are two types of seamless GNGs along the shock direction: negative gradient structure with grain size from large to small (S1); positive gradient structure with grain size from small to large (S2). The particle velocities analyzed in current study are in the whole range from 0.5 to 5 km/s. As a comparison, we also created two homogeneous samples: homogeneous nanoglass with a grain size of 8 nm (S3), homogeneous $Cu_{64}Zr_{36}$ MG (S4). Section 2 describes the methodologies, including the model constructions, shock simulations, and necessary physical parameters. Section 3 discusses the simulation results and explains their mechanisms of physics and mechanics. Finally, the relevant innovations are concluded in Section 4.

2. Methodologies

2.1. Sample constructions

All large-scale MD simulations are carried out using the simulation package LAMMPS (large-scale atomic/molecular massively parallel simulator)(Hammond, 2020) to explore the shock responses of $Cu_{64}Zr_{36}$ GNGs and homogeneous samples. The embedded-atom method (EAM) potential developed by Mendelev et al.(Mendelev et al., 2019) is adopted for atomic interactions of Cu and Zr. This EAM potential made some reasonably semiempirical corrections is currently the latest to simulate Cu-Zr MGs. Therefore, this EAM potential is a more suitable and reasonable one to describe the Cu-Zr glass system.

Figs. 1(a-e) display the process of establishing nanoglasses with linear and monotonous gradient structure. First, a small-scale cubic $Cu_{64}Zr_{36}$ bulk MG sample containing 82,600 atoms (the side length of ~10 nm) is generated with the 3D periodic boundary conditions. The annealing time and temperature are set to be 1000 ps and 2000 K, respectively. The melting/quenching rate of 10 K/ps is selected to build the MG samples because this rate can form glass by inhibiting crystallization(Demaske et al., 2018; Feng et al., 2016; Huang et al., 2014; Jian et al., 2015; Ma et al., 2017; Tang et al., 2019; Wen et al., 2018). Subsequently, the small-scale $Cu_{64}Zr_{36}$ MG sample is replicated to generate a larger sample, as shown in Fig. 1(a). After replication, the size of large-scale $Cu_{64}Zr_{36}$ MG is approximately 30 (X) ×30 (Y) ×200 (Z) nm^3, with a total of 14,868,000 atoms. The large-scale $Cu_{64}Zr_{36}$ MG sample is further annealed for 200 ps at a temperature (700 K) near the glass transition temperature T_g. The value of T_g is 800 K for the $Cu_{64}Zr_{36}$ MGs(Demaske et al., 2018). After that, the sample is quenched again to 50 K and relaxed for 100 ps. All above MGs' constructions (melting, quenching, annealing, and relaxation) are performed with a MD integration timestep of 1 fs and an external hydrostatic pressure of 0 GPa.

The nano-scale grains in nanoglasses are generated by the Voronoi tessellation method sprinkling random points in samples. The seed sample of grain is the large-scale MG presented in Fig. 1(b). In constructing the initial gradient nanoglass (GNG), these points

follow a well-designed density defined to establish the aimed gradient for grain size. The density of points is designed by specifying an average distance of all points in a specific region, following the gradient function $a(\overline{Z} - \overline{Z}^2)^{3/2} + b$ in the Z-direction. Where a and b are constants, $\overline{Z}$ represents the scaled positions along the Z-direction, i.e., $0 \leq \overline{Z} \leq 1$. The actual value range of Z in the initial GNG is [0, 200 nm]. The size of the initial GNG sample $(30 \times 30 \times 200 \text{ nm}^3)$ is the same as that of the large-scale MG. It should be noted that each grain must maintain a distance of 1 Å from grain interfaces when it is filled, because the atoms need to avoid overlapping at grain interfaces. In addition, after the initial GNG is established, all atom pairs whose distance is less than 2.2 Å were searched, and then one of the two atoms is deleted. The selected distance of 2.2 Å is based on the radial distribution function in the large-scale $Cu_{64}Zr_{36}$ MG. In Fig. 2, the nearest average interatomic distances of Cu-Cu, Cu-Zr, and Zr-Zr pairs are 2.48 Å, 2.79 Å, and 3.18 Å, respectively, which are in good agreement with the experimental measurements ($r_{Cu-Cu} = 2.48$ Å, $r_{Cu-Zr} = 2.72$ Å, and $r_{Zr-Zr} = 3.12$ Å)(Babanov et al., 1995; Chen and Waseda, 1979; Eckert et al., 2007; Kim and Lee, 2008; Laridjani and Sadoc, 1988; Mattern et al., 2008; Mendelev et al., 2009; Păduraru et al., 2007). These data prove the reliability of the EAM potential used currently to some extent. The grain sizes (average diameter d_{ave}) in the initial GNG vary first from 12 to 3 nm, and then from 3 to 12 nm in a seamless way, following an approximately linear structure, as displayed in Fig. 1(c). To minimize the initial porosity caused by deleting atoms, the initial GNG is relaxed by imposing an external pressure of 3 GPa at 50 K for 200 ps. After that, the sample is relaxed again at zero pressure and 50 K for 200 ps to equilibrate atomic structure. Here, the low temperature (50 K) is used to avoid thermal activation of structural rearrangement on the interface since micro glass structures after rapid quenching are more prone to undergo thermal activation than the macro amorphous structures that experience a longer period of relaxation in the real world(Cheng et al., 2008b). Finally, the initial GNG is cut in the middle to obtain two monotonous linear GNGs. The one is a negative gradient sample (S1) decreasing grain sizes along the shock direction (Fig. 1(d)). The other is a positive gradient sample (S2) with increasing grain sizes in the positive Z-direction (Fig. 1(e)). Moreover, we also construct two homogeneous samples as a comparison: homogeneous nanoglass with a grain size of 8 nm (S3) and homogeneous $Cu_{64}Zr_{36}$ MG (S4). The dimensions of the homogeneous samples (S3, S4) are the same as those of the S1 and S2 samples.

2.2. Shock simulation setup

All samples are relaxed again at 50 K for 100 ps to ensure systems are well equilibrated. Then, we reset the Z-direction to free boundary but maintain periodicity in other directions. The shock simulations are carried out under the microcanonical ensemble (i.e., NVE). Subsequently, the planar shock wave is generated by a flat-surface infinite-mass wall at the lowest Z position that moves toward the positive Z-direction (from left to right). To make all samples (S1, S2, S3, and S4) comparable with different shock strengths, the duration of each simulated shock pulse is kept constant at 15 ps. After the wall is removed, the initial unloading wave appears at the left end of the sample. Moreover, the shock pulse continues to propagate toward the right side, and forms a new wave reflected into the sample when it reaches the rear surface. As time goes by, the reflected wave and initial unloading wave will encounter and interact. Their interaction creates a tensile stress state at the corresponding site in a sample. As long as the spall strength of the material is exceeded by tensile stress, the spall fracture will be triggered. To conduct a complete study of shock response, the particle velocities analyzed currently are in the entire range from 0.5 to 5 km/s. The timestep used in our shock simulations is also set to 1 fs.

To characterize and compare shock responses, the gradient and homogeneous samples are divided into a large number of bins in the Z-direction. The local physical quantities (the shear strain, stress, configurational entropy, temperature, etc.) are averaged in each bin. Here, the width of the bin is set to 6 Å to ensure a low fluctuation.

2.3. Physical parameters calculation

To analyze the atomic movement and rearrangement during shear deformation in amorphous samples, the von Mises shear strain η_i^{Mises} of each atom needs to be calculated by the following steps(Shimizu et al., 2007). First, there are two configurations (reference and current) required for the calculation of η_i^{Mises}. For shock simulations, the reference configuration is generally the unshocked sample.
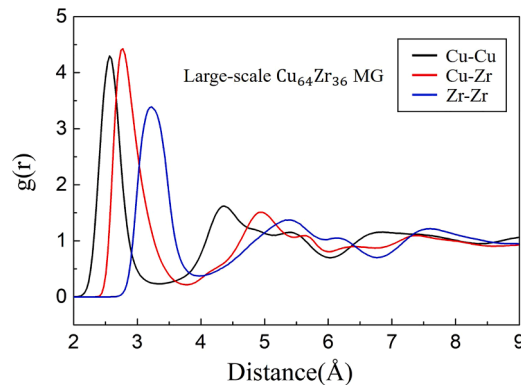

Fig. 2. The radial distribution function of large-scale $Cu_{64}Zr_{36}$ MG.

Secondly, determining the local transformation matrix J_i that maps the following relationship:

$$\left\{d_{ji}^0\right\} \to \{d_{ji}\}, \ \forall j \in N_i^0 \tag{1}$$

where superscript 0 represents the reference configuration, d_{ji} is the separation (row) vectors. The N_i^0 denotes the total number of nearest neighbors of atom i with a given cutoff distance. Here, the cutoff distance is set to 4.6 Å in this work. Minimizing the result in Eq. (2), the J_i can be determined.

$$\sum_{j\in N_i^0}\left|d_{ji}^0 J_i - d_{ji}\right|^2 \tag{2}$$

The strain matrix η_i for each atom is computed as:

$$\eta_i = 1/2\left(J_i J_i^T - I\right) \tag{3}$$

where T and I denote the transpose, and identity matrix, respectively. Finally, the η_i^{Mises} for each atom is calculated by Eq. (4):

$$\eta_i^{Mises} = \left\{1/6\left[\left(\eta_{xx} - \eta_{yy}\right)^2 + \left(\eta_{yy} - \eta_{zz}\right)^2 + \left(\eta_{zz} - \eta_{xx}\right)^2 + \eta_{xy}^2 + \eta_{yz}^2 + \eta_{zx}^2\right]\right\}^{1/2} \tag{4}$$

where η_{ij} is the strain components for each atom.

Here, we also focus on the shock response of some non-equilibrium thermodynamics in nanoglasses, i.e., stress, configurational entropy, and temperature. According to the virial formula of Eq. (5)(Shao et al., 2018), the stress tensor (σ_{xx}, σ_{yy}, σ_{zz}, τ_{xy}, τ_{xz}, τ_{yz}) of each atom can be given:

$$\sigma_{\alpha\beta} = -1\left/ \Omega_i \left(\sum_i m_i v_{i\alpha} v_{i\beta} + \sum_i \sum_{i>j} r_{ij\alpha} f_{ij\beta}\right)\right. \tag{5}$$

where $\alpha(\beta)$ denotes X, Y, or Z axes, m_i and v_i represent the mass and velocity of atoms i, and f_{ij} is the force between atoms i and j. Ω_i is the current volume of the atoms i. It should be pointed out that in this work, the shock stress is recognized as the σ_{zz} (or σ_{33}). Besides, the first term of Eq. (5) is a contribution only from thermal kinetic energy, so the translational velocity of the centroid of each bin is subtracted in the v_{iz}. The maximum shear stress (deviatoric shear stress) used in our analysis is defined as:

$$\tau = 1/2\left(\sigma_{zz} - 1/2\left(\sigma_{xx} + \sigma_{yy}\right)\right) \tag{6}$$

The configurational entropy on atom i can be achieved using the Eq. (7)(Piaggi and Parrinello, 2017):

$$s_S^i = -2\pi\rho k_B \int_0^{r_m}\left[g_m^i(r)\ln g_m^i(r) - g_m^i(r) + 1\right]r^2 dr \tag{7}$$

where ρ represents the system's density, k_B is Boltzmann constant. g_m^i denotes the radial distribution function centered at the i-th atom and can be calculated as follow:

$$g_m^i(r) = \frac{1}{4\pi\rho r^2}\sum_j \frac{1}{\sqrt{2\pi\sigma^2}}e^{-(r-r_{ij})^2/(2\sigma^2)} \tag{8}$$

where the sum in j goes through the neighbors of atom i, and σ is a broadening parameter rather than stress. It is worth noting that the system of the ρ and $g_m^i(r)$ should be the bin where the atom i is located instead of the entire sample.

The temperature of each bin, generally, is calculated by the Eq. (9)(Hahn et al., 2017):

$$T = 1\left/ 3N k_B \sum_{i=1}^N m_i\left(v_{ix}^2 + v_{iy}^2 + v_{iz}^2\right)\right. \tag{9}$$

where m_i denotes the atomic mass, k_B represents Boltzmann constant, and v_{ix}, v_{iy}, v_{iz} are the components of atomic velocity. For shock simulations, a reasonable calculation of the temperature also needs to subtract the translational velocity of the centroid of each bin in the shock direction. However, this method is not adopted. For more accurate and concise calculations in this work, the temperature equation is modified to 2D as the following:

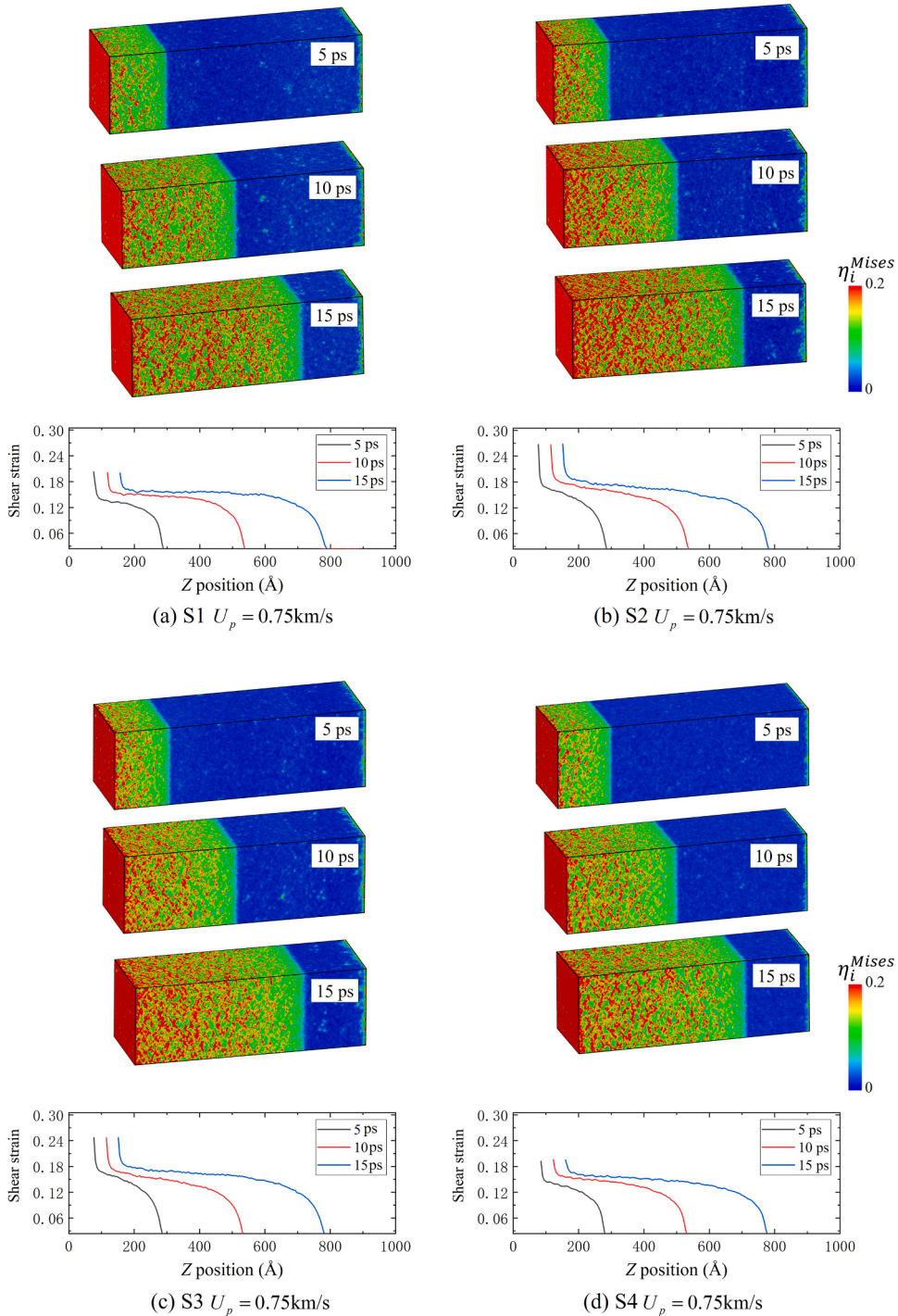$$T = 1\left/ 2N k_B \sum_{i=1}^N m_i\left(v_{ix}^2 + v_{iy}^2\right)\right. \tag{10}$$

Fig. 3. The detailed visualization of internal shear deformation at $U_p = 0.75$ km/s. (a) S1. (b) S2. (c) S3. (d) S4. The above is the atomic schematic of von Mises shear strain η_i^{Mises} in the samples at different shock timesteps. Below them, there are shear strain profiles along the shock direction (Z-axis). The local shear deformation is calculated by averaging the atomic η_i^{Mises} in a sphere region with a radius of 0.64 nm.

3. Results and discussion

3.1. The effects of gradient on shock-induced plasticity

3.1.1. Shear strain

Fig. 3 shows the detailed visualization of internal shear deformation at $U_p = 0.75$ km/s. In MD simulations, the atoms with η_i^{Mises} higher than 0.2 are thought to undergo plastic shear deformation in MGs, so a large number of shear transformation zones (STZs) can be identified by assigning colors to atoms(Falk and Langer, 2011). Generally, the density of STZs is proportional to the degree of shear deformation. It is evident that the gradient structure has a significant effect on the shear deformation behavior in nanoglasses. The density of STZs in the S1 sample is far less than that in the S2 sample at the same moment (5 ps, 10 ps, and 15 ps). Moreover, as shock pulse continues, the STZs in a region that shock wave has swept are still increasing for all samples. These phenomena are also reflected in the shock wave profiles of shear strain. It was already clarified that the STZs in the region swept by shock waves continue to increase. Besides, the action time of shear stress gradually decreases in the positive Z-direction due to shock wave propagation. Therefore, the shear strain of homogeneous samples (S3, S4) decreases progressively along the shock direction. Interestingly, the shear strain, at 10 ps and 15 ps, is approximately uniformly distributed in the S1 sample, as presented in the lowest Fig. 3(a). Thus, the rate of shear deformation in the S1 sample increases along the shock direction (Z-axis). For the S2 sample, the shear strain also decreases along the shock direction at each moment, as displayed in the lowest Fig. 3(b). However, its decreasing trend is stronger than that of homogeneous samples. These results indicate that the shear deformation rate in the S2 sample decreases in the positive Z-direction.

In light of the above characteristics of STZs, it can be concluded that the shear deformation of nanoglasses during shock is closely related to grain sizes. The shear deformation rate of nanoglasses increases with decreasing grain size. Moreover, the degree of shear deformation also increases as the grain size decreases. To study the causes of these phenomena, it is necessary to analyze the atom configuration of nanoglasses.

As it is known, the atomic configuration of conventional polycrystals has vast differences between grain interiors and boundaries. With the exception of a few coherent or semi-coherent interfaces, the atoms at grain boundaries are generally in a disordered structure and can be recognized by the common number analysis (CNA)(Liu et al., 2019). For nanoglasses, however, both grain interiors and interfaces lack atomic periodicity in the long-range (amorphous structures)(Adibi et al., 2014). Therefore, the CNA does not work to identify glass-glass interfaces in nanoglasses. Recently, Pan et al.(Pan et al., 2015) propose a quasi-nearest atom (QNA) parameter to characterize interfaces in nanoglasses based on a lower atomic packing density in grain interfaces. The QNA can directly distinguish the local atomic environment by forming a contrast in grain interiors and interfaces. A higher atomic QNA (N_Q) corresponds to a looser atomic packing. Fig. 4 shows the separation of the dominant grain interfaces from the grain interiors in the unshocked samples. To be more intuitive, the unshocked samples (S1, S2, S3, S4) are first sliced with a thickness of 1 nm along the shock direction. Then, the atoms in slices are colored with N_Q. The atoms with N_Q smaller than 6 belong to the grain interiors (blue), whereas those larger than 6 pertain to the grain interfaces (light blue). After separation, the thickness of grain interfaces is approximately 1.0-1.5 nm. Moreover, there are no grain interfaces in the S4 sample, thus all the atoms in S4 belong to grain interiors in the subsequent analysis.

Fig. 5 presents the fraction of atoms in the grain interiors or interfaces as functions of Z position in the unshocked gradient and homogeneous nanoglasses. The red lines represent density distribution. For the GNGs (S1, S2), the atomic fraction of grain interfaces significantly increases as the grain size decreases, but the density decreases. In the homogeneous nanoglass (S3), the density remains basically stable along the shock direction. Theoretically, in an amorphous structure, a decrease in density is equivalent to an increase in free volume. Therefore, the grain interfaces in nanoglasses have a higher free volume than the grain interiors. The deformation behavior in an amorphous sample is mainly determined by the mutual competition between the free volume generation and annihilation(Spaepen, 1977). Moreover, a higher free volume also leads to a faster rate of deformation(Turnbull and Cohen, 1961). Thus, the difference in local shear deformation rate in the GNGs is primarily due to a change in free volume along the shock direction. In the next part of this section, the reasons for the higher free volume of grain interfaces will be discussed in detail by the chemical short-range order, i.e., atomic Voronoi polyhedral (VP) clusters(Feng et al., 2015).

Feng et al.(Feng et al., 2015) pointed out that the Voronoi index $<n_3, n_4, n_5, n_6>$ can be used to characterize the VP clusters, where n_i denotes the number of i-bonded atoms on clusters. However, this characterization method is not intuitive. Therefore, we have
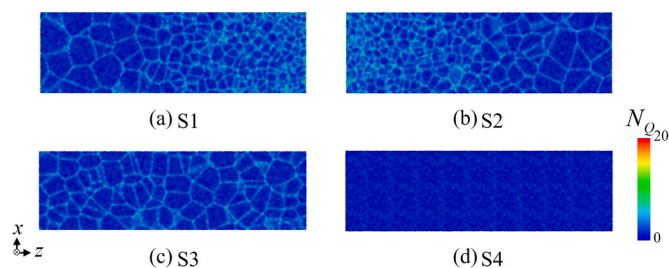

Fig. 4. Separation of the dominant grain interfaces from the grain interiors in a slice of unshocked samples, characterized with a parameter termed quasi-nearest atom (QNA) that is larger than 6. (a) S1. (b) S2. (c) S3. (d) S4. The atomic QNA (N_Q) is averaged in a neighbor region with a radius of 0.64 nm.
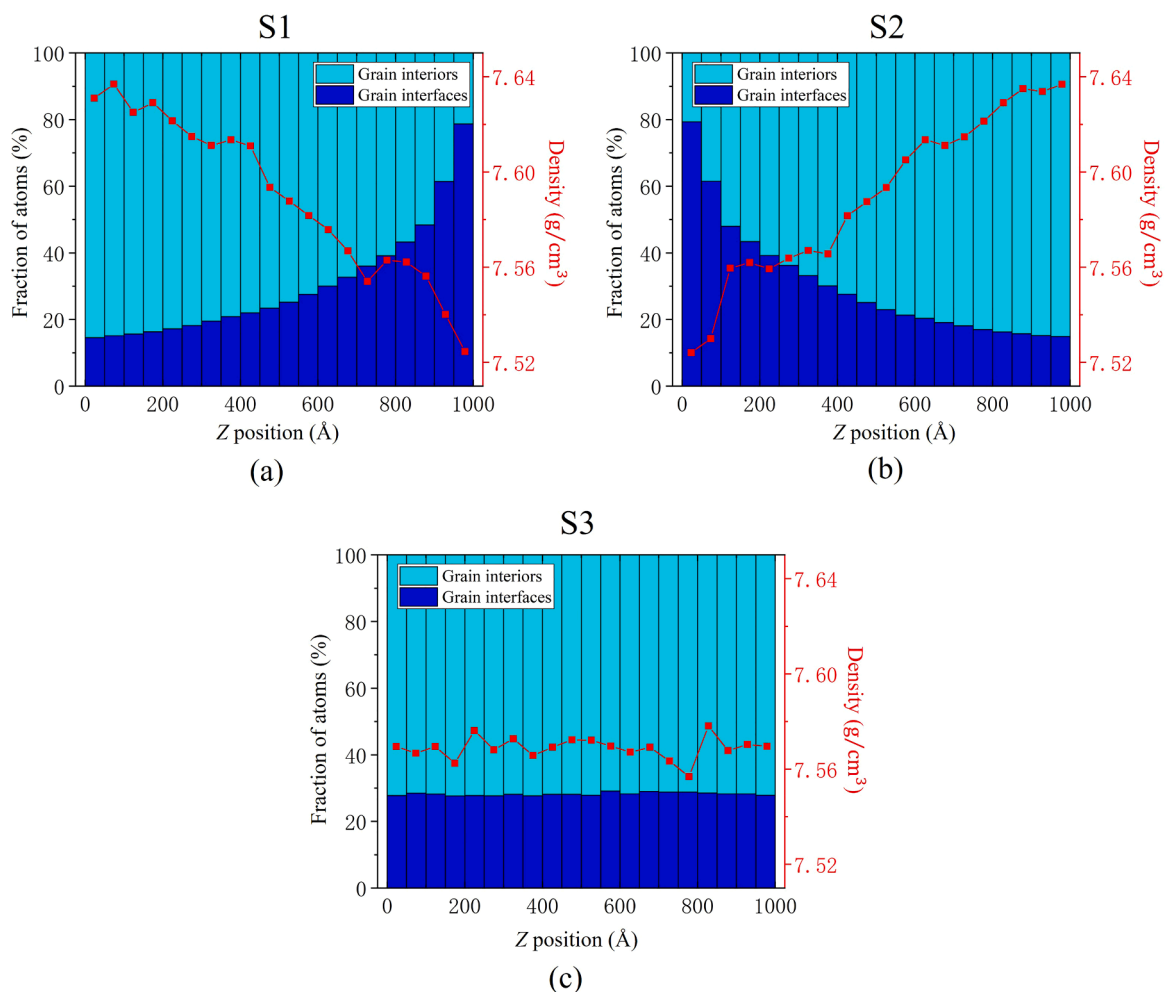
Fig. 5. The fraction of atoms in the grain interiors or interfaces as functions of Z position in the unshocked gradient and homogeneous nanoglasses. The red lines represent density distribution in the samples. (a) S1. (b) S2. (c) S3.
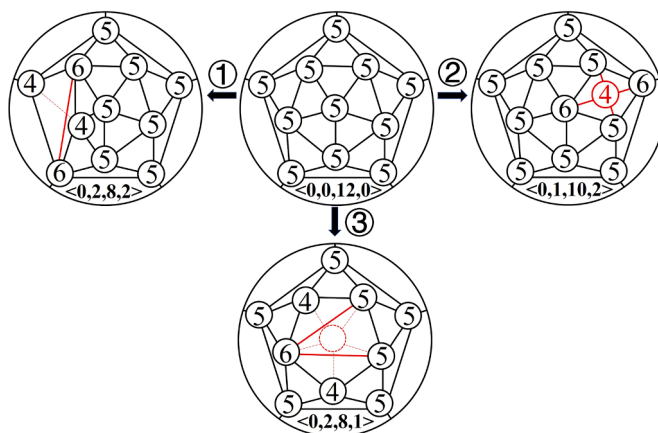

Fig. 6. Schematic of the transformations of the icosahedron-like clusters. The red lines denote the changes of clusters after transformations. Solid lines are the part added, while dashed lines are that disappeared.

proposed the stereographic projection method(Guan et al., 2021) in our previous work to intuitively show the VP clusters. In terms of multiple types of VP clusters in MGs, the <0,0,12,0> clusters have the highest degree of regularity and fivefold symmetry, which are called the perfect icosahedral clusters. Moreover, we also found that some clusters' structures are very similar to the <0,0,12, 0> clusters because they can be transformed from simple structural changes of the <0,0,12,0> clusters. Thus, these VP clusters can be named the icosahedron-like clusters. Fig. 6 displays the transformations of icosahedron-like clusters by the stereographic projection method. As it is known, the simplest structure transformations have three main mechanisms: ① changing a pair of atomic bonds between shell atoms; ② obtaining a shell atom on cluster; ③ losing a shell atom on cluster. As shown in Fig. 6, the <0,0,12,0> clusters can be transformed into <0,2,8,2>, <0,1,10,2>, and <0,2,8,1> clusters by the mechanisms of ①, ②, and ③, respectively. These clusters not only still have a high degree of local fivefold symmetry, but also retain most of the connection characteristics of the <0,0, 12,0> clusters. This fully shows that the structures of these three clusters are highly similar to the <0,0,12,0> clusters. Therefore, the <0,2,8,2>, <0,1,10,2>, and <0,2,8,1> clusters are the icosahedron-like clusters.

Fig. 7 displays the fractions of center atoms for various clusters in the grain interiors and interfaces of S1, S2, S3, and S4 samples. There is no doubt that the perfect icosahedral clusters (<0,0,12,0>) dominate the $Cu_{64}Zr_{36}$ amorphous structure. However, their number in grain interfaces is significantly less than grain interiors. For the icosahedron-like clusters, the significant difference between grain interiors and interfaces is mainly manifested in the <0,1,10,2> clusters. In the non-icosahedral clusters, the difference between grain interiors and interfaces is not significant. Therefore, the fractions of <0,0,12,0> and <0,1,10,2> clusters in the grain interfaces generated by the cold compaction method are significantly less than those in the grain interiors produced by the annealing process.

To analyze the influence of <0,0,12,0> and <0,1,10,2> clusters on free volume in detail, the atomic-packing efficiency (APE), which is one of the main structure parameters for VP clusters, needs to be investigated. The APE's equation was proposed by Yang et al. (Yang et al., 2012) to characterize the space utilization of VP clusters:

$$\eta = 1 \left/ n \sum_{i=1}^{n} \frac{V_{ia}}{V_{iu}} \right. \tag{11}$$

where n is the total number of a certain type of VP clusters, V_{ia} and V_{iu} denote the volume of the embedded atoms inside the i-th cluster, and the total volume of the i-th cluster itself, respectively. The detailed calculations of the V_{ia} and V_{iu} can be found in Ref. (Yang et al., 2012). Based on the above definition, a higher value of η indicates that this cluster has a better space utilization and lower atomic Voronoi volume.

Table 1 summarizes the APEs of <0,0,12,0> and icosahedron-like clusters in the grain interiors and interfaces of GNGs (S1 and S2) and homogeneous samples (S3 and S4). Here, the APEs of icosahedron-like clusters show a weaker difference, so these clusters' APEs are averaged to reduce calculation cost. As a comparison, the average APEs of all clusters are also calculated in Table 1. It is apparent from this table that the APEs of icosahedron-like clusters in grain interiors and interfaces tend to be similar to those of <0,0,12,0> clusters, regardless of whether they are Cu-centered or Zr-centered. This further indicates that the atomic microstructure of icosahedron-like clusters is indeed close to <0,0,12,0> clusters. Moreover, the APEs of both <0,0,12,0> and icosahedron-like clusters are higher than the average APEs of all clusters. Thus, the atomic Voronoi volume in <0,0,12,0> and icosahedron-like clusters is relatively small. In previous studies(Feng et al., 2014), the <0,0,12,0> clusters were found to be a key structure to resist shear deformation in a Cu-Zr MG. Based on the current analysis of APEs, the reason for the high shear resistance of <0,0,12,0> clusters is their better space utilization, so they are more difficult to atomic displacement. Finally, in the nanoglasses (S1, S2, and S3), the average APEs of all clusters in grain interfaces are lower than those in grain interiors, which indicates the Voronoi volume of atoms in grain interfaces is relatively large. As proved above, the atomic Voronoi volume of <0,0,12,0> and <0,1,10,2> clusters is smaller. The
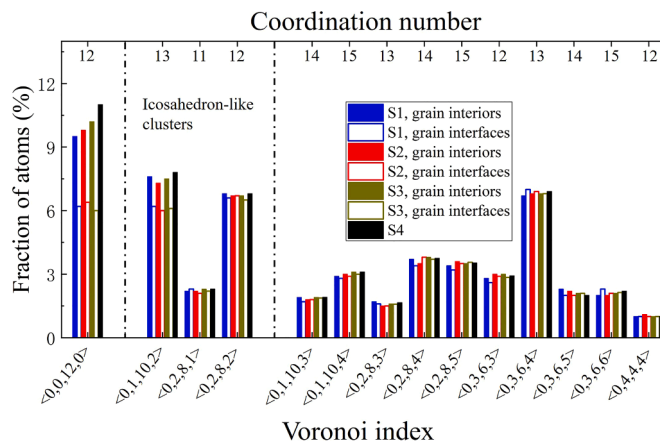

Fig. 7. The fractions of center atoms for various clusters in the grain interiors and interfaces of S1, S2, S3, and S4 samples. The coordination number of various clusters is marked on the top. The left is perfect icosahedral clusters; the center is icosahedron-like clusters; the right is non-icosahedral clusters.

Table 1

The atomic-packing efficiency (APE) of <0,0,12,0> and icosahedron-like clusters in the grain interiors and interfaces of GNGs (S1 and S2) and homogeneous samples (S3 and S4). The average APEs of all clusters are also calculated.

Sample		Clusters	Atomic-packing efficiency (%)	
			Zr-centered	Cu-centered
S1	Grain interiors	<0,0,12,0>	72.54	68.42
		Icosahedron-like clusters	72.16	68.08
		All clusters	71.37	67.69
	Grain interfaces	<0,0,12,0>	72.33	68.41
		Icosahedron-like clusters	71.96	68.01
		All clusters	70.54	67.14
S2	Grain interiors	<0,0,12,0>	72.55	68.42
		Icosahedron-like clusters	72.11	68.11
		All clusters	71.28	67.66
	Grain interfaces	<0,0,12,0>	72.41	68.34
		Icosahedron-like clusters	72.01	68.11
		All clusters	70.65	67.12
S3	Grain interiors	<0,0,12,0>	72.63	68.22
		Icosahedron-like clusters	72.24	68.04
		All clusters	71.25	67.46
	Grain interfaces	<0,0,12,0>	72.51	68.23
		Icosahedron-like clusters	72.12	68.13
		All clusters	70.35	67.26
S4	Bulk MG	<0,0,12,0>	72.71	68.62
		Icosahedron-like clusters	72.41	68.33
		All clusters	71.49	67.87

relatively low fractions of these two types of clusters in grain interfaces cause the average Voronoi volume of atoms to rise inevitably. According to the researches of Turnbull et al.(Turnbull and Cohen, 1961), the free volume in amorphous structures can increase with the Voronoi volume because of the constant volume of atoms. Therefore, the reason for the higher free volume in grain interfaces is the fractions of <0,0,12,0> and <0,1,10,2> clusters are relatively lower.

3.1.2. Stress

Fig. 8 shows the shock stress and shear stress (σ_{33}, and 2τ) profiles as functions of Z position at different time with the particle velocities of 0.5 km/s, 1.0 km/s, and 1.5 km/s. Clearly, the gradient structures affect the stress waveforms, and this is especially significant under weak shocks. For the S1 sample, at $U_p = 0.5$ km/s, the σ_{33} on the left side at 10 and 15 ps is higher than that at 5 ps. Previous studies(Li et al., 2020) on polycrystalline showed that when the grain size is larger, the shock stress is slightly higher. Therefore, the larger grain size may increase the shock stress of nanoglasses to some extent. Besides, it was already clarified that the shear deformation rate on the left side of the negative gradient structure is weak. Theoretically, during shear deformation, a lower rate results in a weaker relaxation of stress. Finally, the shock stress will also slightly increase after the shear deformation stabilizes. In Fig. 8(a), the shear stress on the left side tends to be stable at 10 and 15 ps. Therefore, the σ_{33} on the left side of the S1 sample rises at 10 and 15 ps. It can also be noticed that there is a discernable two-wave structure at 15 ps. However, the two-wave structure is caused by the difference in shear deformation rate rather than the separation of elastic precursor and plastic wave. As mentioned earlier, the shear deformation rate in the GNGs increases with the decrease of grain size. The shear stress quickly increases to the maximum as the shock front sweeps through, and then decreases gradually. During the decrease of shear stress, a higher shear deformation rate corresponds to a lower σ_{33}. For the S2 sample, at $U_p = 0.5$ km/s, the σ_{33} on the left side at 10 and 15 ps is lower. The σ_{33} gradually increases along the shock direction because the positive gradient structure makes shear deformation more and more difficult. For the homogeneous samples (S3 and S4), at $U_p = 0.5$ km/s, the σ_{33} basically maintains stable in the Z-direction because there is no gradient structure causing local differences in grain size and shear deformation rate. However, the S4 has a higher σ_{33} than the S3. Therefore, the nanoglasses reduce the shock stress of MGs under weak shocks.

As the shock strength increases ($U_p = 1.0$ km/s, 1.5 km/s), the shock stress (σ_{33}) profiles gradually become flat for all samples. The reason for this phenomenon is the decrease rate of shear stress increases with shock strength, as displayed in Fig. 8. Moreover, after the shear deformation stabilizes, the shock stress is not very sensitive to grain size under strong shocks. Therefore, the shear deformation in the local region swept by the shock front quickly reaches a stable state under strong shocks, which means the difference of shear deformation rate in the gradient structures is difficult to reflect in stress.

3.1.3. Configurational entropy

Fig. 9 shows the configurational entropy profiles as functions of Z position at different time with the particle velocities of 0.5 km/s, 1.0 km/s, and 1.5 km/s. Theoretically, the size and structure of the local region that has undergone shear transformation strongly affect the configurational entropy (or degree of structural orderness) of MGs(Falk and Langer, 1998). In other words, a higher STZs density (shear strain) in a local region has a higher configurational entropy. As shown in Fig. 3, the STZs densities of all samples at the shock site are higher, so all configurational entropy waveforms present a peak on the left. Importantly, the gradient structures significantly affect the configurational entropy waveforms. In the case of $U_p = 0.5$ km/s, the configurational entropy of S1 at the shock front
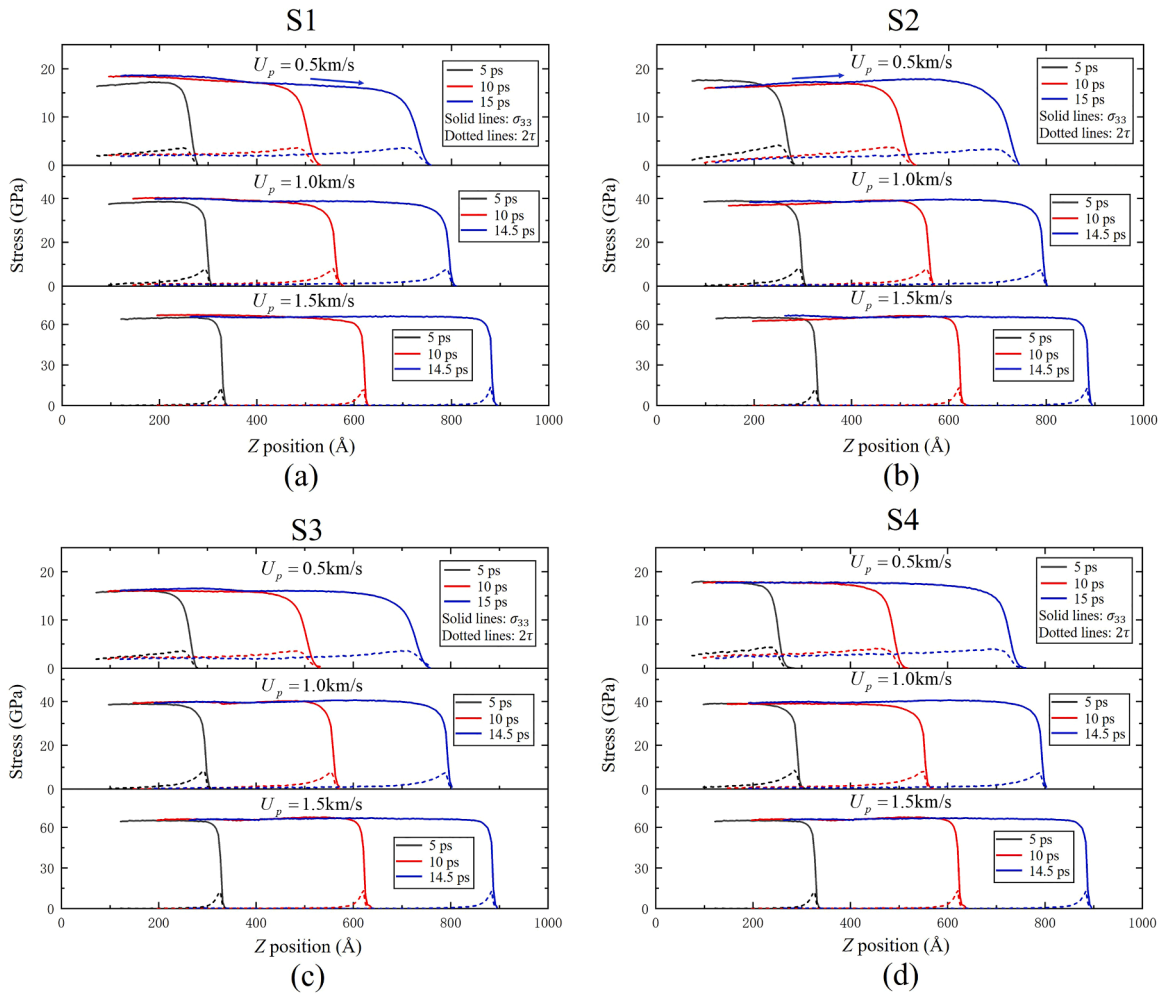
Fig. 8. Shock stress profiles as functions of Z position at different time with the particle velocities of 0.5 km/s, 1.0 km/s, and 1.5 km/s. (a) S1. (b) S2. (c) S3. (d) S4. The solid lines refer to shock stress σ_{33}. The dotted lines denote double maximum shear stress 2τ.

gradually increases during propagation, while that of S2 progressively decreases. It was already clarified that the gradient structures make the local shear deformation rate different. Moreover, the shear deformation at the shock front is in the initial stage. Therefore, the shear deformation rate is also one of the factors that affect the configurational entropy. During shear deformation, a relatively higher rate will cause a higher configurational entropy in an amorphous structure because higher atomic fluctuations increase the degree of confusion in the configuration(Way et al., 2007). For the homogeneous samples (S3 and S4), the configurational entropy at the shock front basically remains constant.

As the shock strength increases ($U_p = 1.0$ km/s, 1.5 km/s), the shear deformation rates of all samples substantially increase, and the time for the shear deformation to reach a steady-state is greatly shortened. When the shear deformation is stable, atoms will be relaxed to a lower stable energy level. This means that the configurational entropy caused by shear deformation rate is relaxed. At this time, the configurational entropy is mainly determined by the degree of shear deformation (density of STZs). Therefore, as the shock front sweeps through, the configurational entropy quickly increases to a maximum, and then decreases gradually to a stable value. A larger grain size corresponds to a smaller stable value because a region with a large grain size has a low density of STZs. Moreover, the decrease rate of configurational entropy increases with shock strength.

3.1.4. Temperature

Fig. 10 displays the shock temperature profiles as functions of Z position at different time with the particle velocities of 0.5 km/s, 1.0 km/s, 1.5 km/s, and 2.0 km/s. Unexpectedly, all temperature waveforms have a peak on the left. These results are related to the shock pattern selected. Generally, there are two methods of generating planar shock waves in a sample: flat-surface rigid piston, and flat-surface infinite-mass wall. For the rigid piston method, the force field of atoms in piston is removed to achieve rigidity, and then the piston is applied with a constant velocity to generate a shock pulse. This method does not cause temperature peak on the shock side (Wen et al., 2019). However, the piston has a weaker ability to confine atoms because of the lack of force field. Therefore, when the U_p
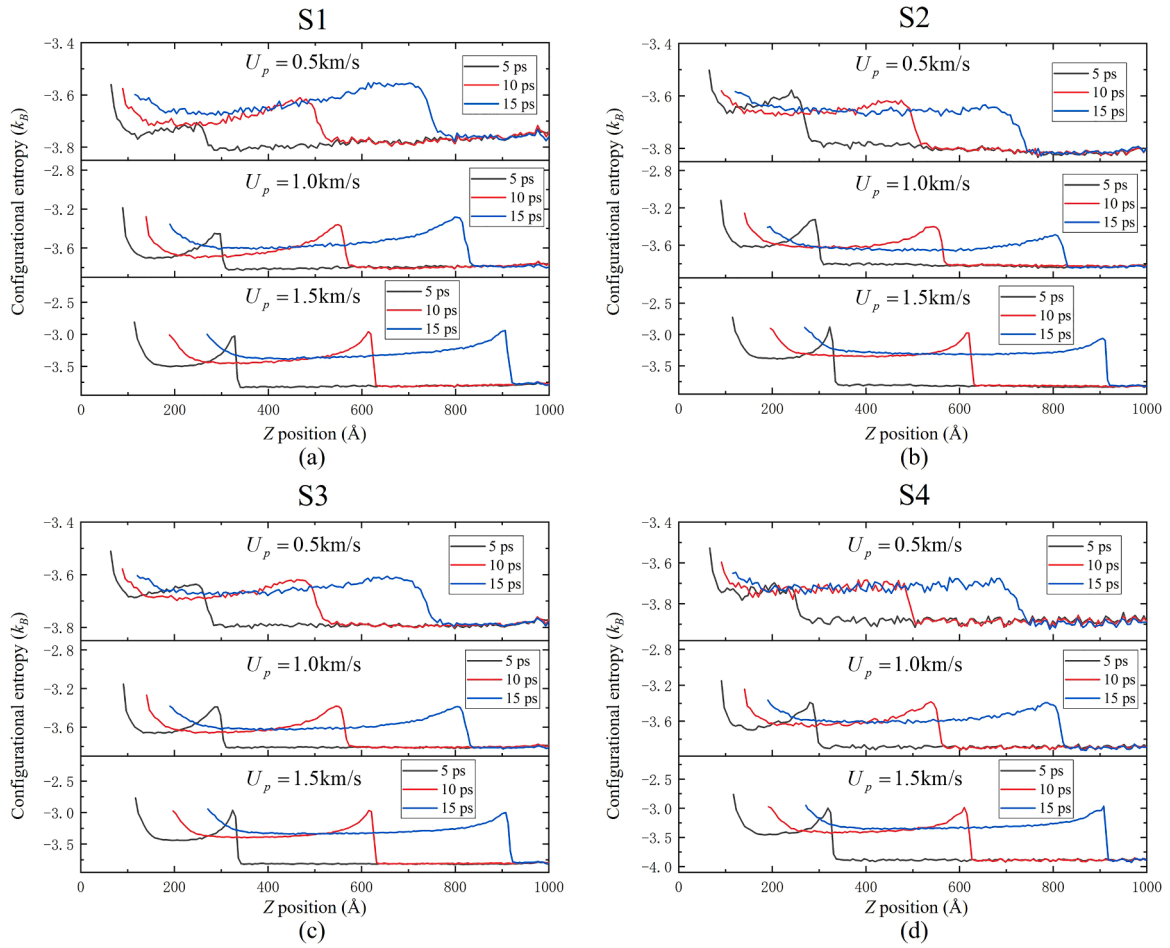
Fig. 9. Configurational entropy profiles as functions of Z position at different time with the particle velocities of 0.5 km/s, 1.0 km/s, and 1.5 km/s. (a) S1. (b) S2. (c) S3. (d) S4. The unit for configurational entropy is Boltzmann constant k_B.

exceeds 2 km/s, the atoms in target may penetrate the piston. The infinite-mass wall does not ignore the force field so that it can generate a higher shock strength. However, the temperature waveform of this method has a peak, caused by the wall's force field, on the shock side. A similar result has also been found in SiC(Li et al., 2019) that uses the infinite-mass wall to achieve shock.

For the S1 sample, in the case of $U_p = 0.5$ km/s, the temperature waveforms show some fluctuations and decrease progressively in the positive Z-direction. At $U_p = 1.0$ km/s, the temperature also decreases along the shock direction. However, when the U_p exceeds 1.5 km/s, the temperature displays an increasing trend in the positive Z-direction ($U_p = 2.0$ km/s). These phenomena indicate that the influence of the negative gradient structure on the temperature waveforms becomes significant only under strong shocks ($U_p > 1.5$ km /s). As discussed previously, the region with a smaller grain size exhibits a faster shear deformation rate. However, due to shock wave propagation, the action time of shear stress is shorter in a smaller grain region for the S1 sample. Therefore, the shear deformation rate and shear stress action time are in competition. Theoretically, the plastic shear deformation in shocked samples will produce an adiabatic temperature rise(Fu et al., 2007). A higher degree of plastic shear deformation (density of STZs) corresponds to a higher temperature. It should be pointed out that the shear deformations in current study are all plastic. Under weak shocks, the effect of the action time is more significant, and the density of STZs increases with the action time. Thus, the temperature profiles decrease in the positive Z-direction. As the shock strength increases, the shear deformation rate increases and the shear deformation reaches the stable state in a shorter time, which gradually weakens the effect of the action time. Besides, the density of STZs after stabilization increases with the decrease of grain size. As a result, the temperature in a smaller grain region is higher under strong shocks. For the S2 sample, however, the shear deformation rate and action time are in a cooperative relationship. The positive gradient structure always shows a significant influence on temperature waveforms. Therefore, the temperature decreases along the shock direction in the S2 sample for all shock strengths. In the homogeneous samples (S3 and S4), the shear deformation degree is only affected by the action time, so the temperature waveforms decrease along the shock direction under weak shocks. However, the effect decreases as the shock strength increases. Thus, the temperature profiles gradually become flat with increasing shock strength.
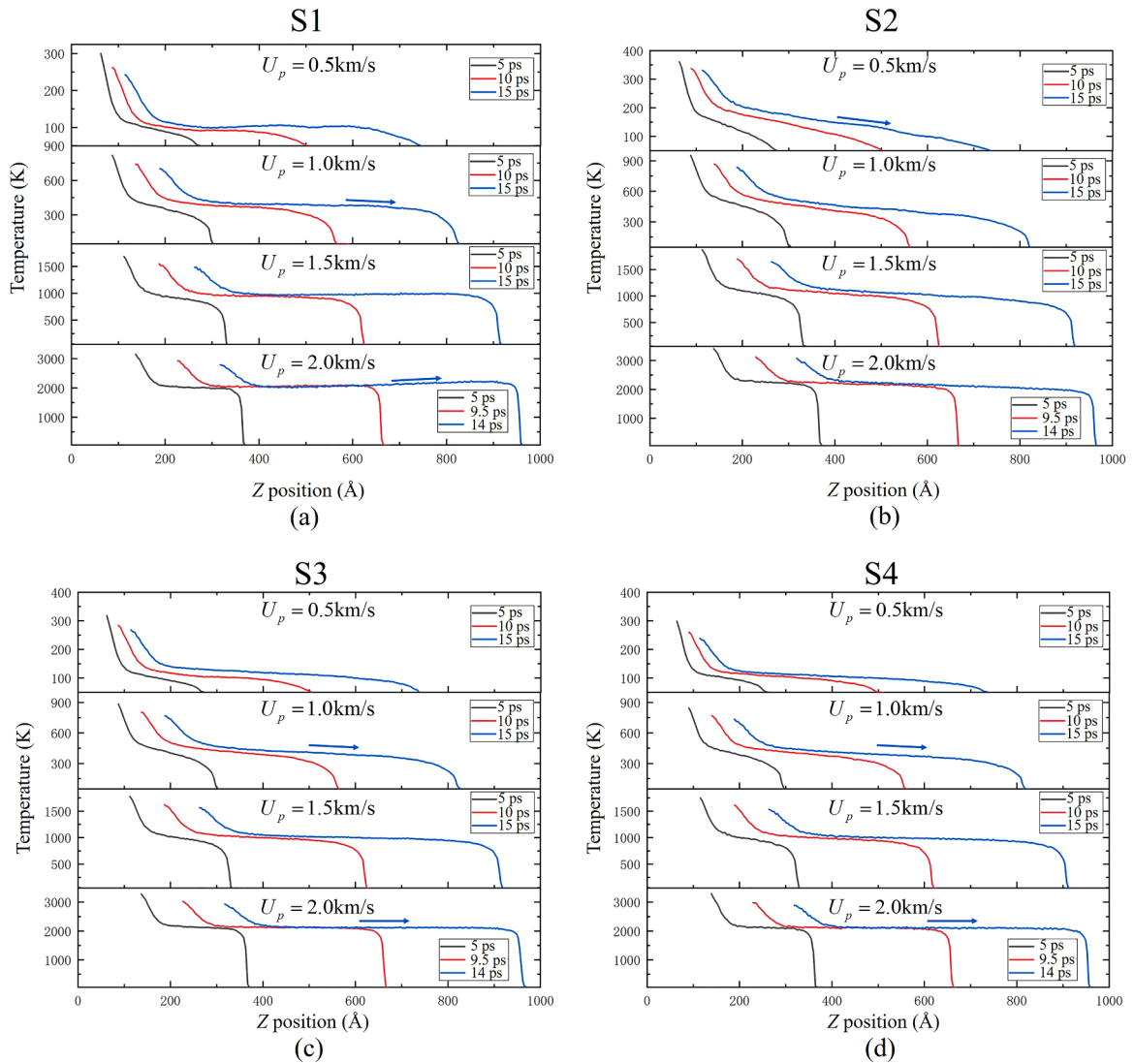
Fig. 10. Shock temperature profiles as functions of Z position at different time with the particle velocities of 0.5 km/s, 1.0 km/s, 1.5 km/s, and 2.0 km/s. (a) S1. (b) S2. (c) S3. (d) S4.

3.1.5. Shock wave speed

Fig. 11 presents the comparison of shock wave speeds in the gradient and homogeneous samples at different time and particle velocities. Interestingly, for $1\ km/s \leq U_p \leq 5\ km/s$, the shock wave speeds (U_s) in the GNGs seem to remain constant because the waves travel roughly the same distance at the same time interval. In addition, the shock wave speeds in the S3 sample (homogeneous nanoglass) are approximately equal to those in the GNGs. Therefore, the grain size of nanoglasses does not have a significant effect on shock wave speed. For conventional polycrystalline, however, the grain size significantly affects the shock wave speed(Li et al., 2020). As it is known, the elastic wave speed (U_e) is constant in a homogeneous sample, and can be calculated by the equation $U_e = \sqrt{E/\rho_0}$, where E is the modulus of elasticity, ρ_0 denotes initial density. Thus, some researchers speculated that the density may affect shock wave speed to some extent(Hamel et al., 2012). In our current study, the grain size affects the density of nanoglasses, but the shock wave speed does not change significantly, so the density is not a decisive factor of the shock wave speed. The change in shock wave speed may be derived from the difference in atom configuration. Generally, the atom configuration in grain interiors is different from that in grain boundaries. The difference in atom configuration naturally leads to a variety in shock wave speed. Moreover, the atomic ratio between grain interiors and boundaries changes with grain size. As the atomic ratio changes, the dynamic competition of shock wave speeds between grain interiors and boundaries determines the final wave speed in the polycrystalline counterpart. For nanoglasses, the atom configurations of the grain interiors and interfaces are all long-range disordered structures. Besides, the difference in chemical short-range order between grain interiors and interfaces is only reflected in the number of the two types of clusters (<0,0,12, 0>, and <0,1,10,2>). The atomic chemically-disordered features of grain interiors and interfaces are similar, so there is no significant
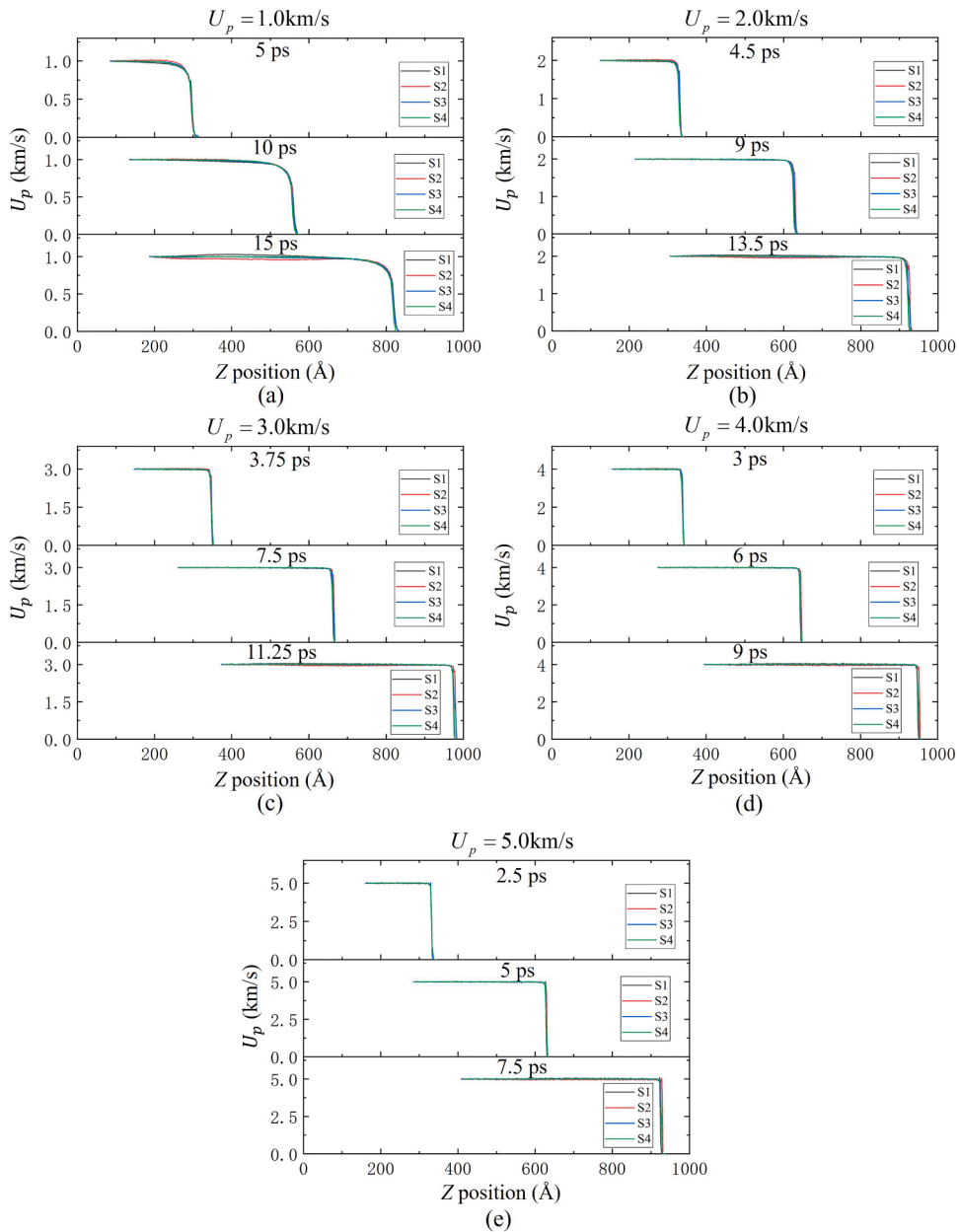
Fig. 11. The comparison of shock wave speeds in the gradient and homogeneous samples at different time. (a) $U_p = 1.0$ km/s. (b) $U_p = 2.0$ km /s. (c) $U_p = 3.0$ km/s. (d) $U_p = 4.0$ km/s. (e) $U_p = 5.0$ km/s.

difference in their shock wave speeds. E.g., the shock wave speeds of the S3 and S4 are basically the same. The glass-glass interfaces do not significantly affect the shock wave speeds of MGs, indicating that the shock wave speed of grain interfaces is similar to that of grain interiors.

3.2. The effects of gradient on spall behavior

Spall behavior is an integral part of the whole shock process, and so far, it is also a critical concern in physics and mechanics. Usually, shock-induced spallation occurs at the site where the initial unloading wave interacts with the reflected wave from the rear surface (free surface). The spallation is a complex thermodynamic process, and its strength is affected by the internal microstructure and external conditions (e.g., atom configuration, grain size, shock stress, temperature, etc.). In this work, two methods are used to calculate spall strengths. The one method directly obtains spall strengths in bulk samples by averaging the tensile stress of atoms at the spall site. The direct method is the advantage of MD and records stress along the shock direction over the whole simulation. The

maximum recorded is generally considered as the spall strength. The other one is an indirect method that is most commonly adopted in shock experiments and simulations. This method uses the velocity evolution of free surface (FS) to calculate spall strengths.

In terms of the direct method, in Eq. (12), a spall strength (σ_{sp}^I) is obtained based on the maximum among average tensile stress of bins subdivided along the shock direction. As detailed in Eq. (13), the indirect method estimates the spall strength (σ_{sp}^F) by the initial density (ρ_0), bulk sound speed (C_b), and "pull-back" velocity (Δu). For the GNGs, the initial density at the nucleated site of the initial void is selected as the ρ_0 used in Eq. (13). The bulk sound speed (C_b) can be calculated by the shock wave speed (U_s) and particle velocity (U_p), as displayed in Eq. (14). The Δu is the most critical item in the indirect method and calculated by the FS velocity evolution, as shown in Fig. 12.

$$\sigma_{sp}^I = \max[\text{stress}(z, t)] \tag{12}$$

$$\sigma_{sp}^F = \frac{1}{2}\rho_0 C_b (u_{max} - u_{min}) = \frac{1}{2}\rho_0 C_b \Delta u \tag{13}$$

$$U_s = C_b + \lambda U_p \tag{14}$$

3.2.1. Spall strength

As discussed in section 3.1.2, the gradient structure makes shock stress unstable, especially when the shock strength is weak. Moreover, the density in the unshocked samples is also affected by the gradient structures. Therefore, the hugoniot data of our GNGs cannot be accurately given. Fortunately, the effect of gradient structures on shock wave speed is not significant. Thus, the bulk sound speed is constant in the GNGs, and the indirect method is still suitable for the analysis of spall strengths. Theoretically, the indirect method is not applicable for traditional polycrystalline with grain size gradient because the inconstant shock wave speed leads to uncertain bulk sound speed and spall site. Fig. 13 shows the shock wave speed as a function of particle velocity in all samples. It is clear that the bulk sound speed is not constant as the particle velocity increases, and all samples have the same bulk sound speed. In our simulations, the bulk sound speed can be divided into two cases in the particle velocity range of 0.5 to 5 km/s. For the former case ($0.5 \text{ km/s} \leq U_p \leq 2.0 \text{ km/s}$), the bulk sound speed evaluated in this work is 3.905 km/s, which is basically consistent with the experimental measurement of bulk MG (3.910 km/s)(Xi et al., 2010). This result proves the reliability of the current shock research data. For the latter case ($2 \text{ km/s} < U_p \leq 5 \text{ km/s}$), the bulk sound speed is 2.967 km/s.

Fig. 14 uses the S3 sample as an example to display the evolution of spallation at $U_p = 1.0$ km/s. There are four typical snapshots of shock stress (σ_{33}) from 26.5 to 32.5 ps in Fig. 14 (a). Moreover, in fig. 14(b), the internal defects (voids and cracks) in sample at the corresponding moment are also presented. The recognition of defects is achieved through the "construct surface mesh" method which sets the probe sphere radius to 0.4 nm(Stukowski, 2014). Based on the radial distribution function of Fig. 2, the radius should select slightly larger than all abscissas of the first peaks, so the 0.4 nm is appropriate. At 26.5 ps, the initial unloading wave encounters the reflected wave from the FS, and then the shock stress begins to shift from compressive to tensile. However, the tensile stress at this moment is not significant, so no defects are generated in sample. As time goes by, the tensile stress in sample gradually increases, and the spall region, dominated by tensile stress, is presented clearly. When the time comes to 30.5 ps, the tensile stress increases to the maximum that the spall region cannot withstand, and some small voids distributed in the center of the spall region are identified. Theoretically, a new FS at this moment is generated inside the spall region. Then, a wave is reflected instantaneously through the new FS, which causes the second increase in FS velocity. The maximum tensile stress at this moment corresponds to the spall strength defined by the direct method. As the time further increases (32.5 ps), the defects increase and grow, resulting in a larger visible band and a rapid decrease in tensile stress. Eventually, the new FS becomes remarkable at the spall site, which causes the sample to be split
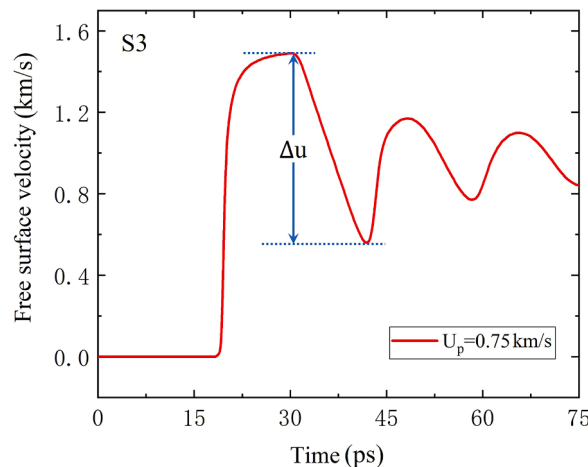

Fig. 12. Illustration of free surface (FS) velocity evolution at $U_p = 0.75$ km/s in the S3 sample.
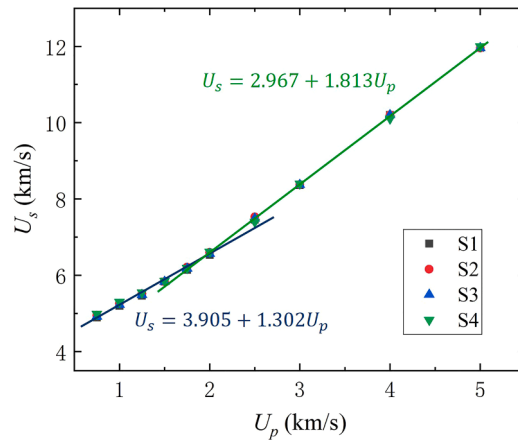
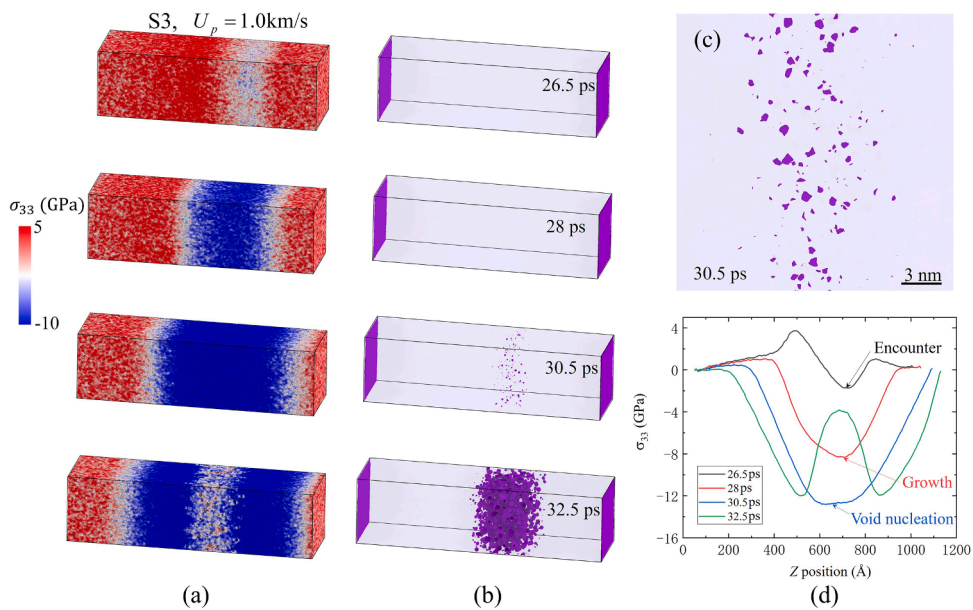**Fig. 13.** The shock wave speed as a function of particle velocity.

Fig. 14. The evolution of classical spallation in the S3 sample at $U_p = 1.0$ km/s. Figures are colored by shock stress (σ_{33}) along the Z-direction (shock from left to right) in the first column (a). The red denotes compression, and the blue is tension. Figures in the second column (b) show the defects recognized by the "construct surface mesh" method. Here, the probe sphere radius is set to be 0.4 nm. (c) The magnified snapshot of the initial nucleation at 30.5 ps. (d) The evolution histories of the shock stress during spallation.

into two parts.

A magnified snapshot of initial nucleation at 30.5 ps is presented in Fig. 14(c). It can be observed that in a narrow region, there are many voids distributed. The existence of many defects indicates that the sample is spalling off. Thus, the tensile stress will gradually decrease in subsequent time. The shock stress profiles at the corresponding moment are shown in Fig. 14(d). At 26.5 ps, the shock stress changes from compressive to tensile in the spall region. At 28 ps, the tensile stress further increases, and the spall region can be observed clearly. When the time is 30.5 ps, the tensile stress, corresponding to defect nucleation, reaches a maximum of 13.11 GPa. After that, a new FS is generated in the sample and splits the tensile stress pulse into two parts. With the increase of time, a large damage field is presented to result in fracture, which makes a sudden drop of the tensile stress.

Figs. 15(a, c, e, g) show the FS velocity evolution of shocked GNGs and homogeneous samples under different particle velocities. For all samples, there is no spallation at $U_p = 0.5$ km/s. Moreover, in the case of $U_p = 5$ km/s, their FS velocities do not appear a pullback. This means that the temperature in the samples is already much higher than the melting point, and the indirect method of calculating spall strength is no longer applicable. In this work, therefore, the comparison of spall strengths between the direct (bulk) and indirect (FS) methods is only in the particle velocity range of 0.75 to 4 km/s.

Figs. 15(b, d, f, h) present corresponding calculated spall strengths from the bulk and FS. It is clear that the spall strengths obtained
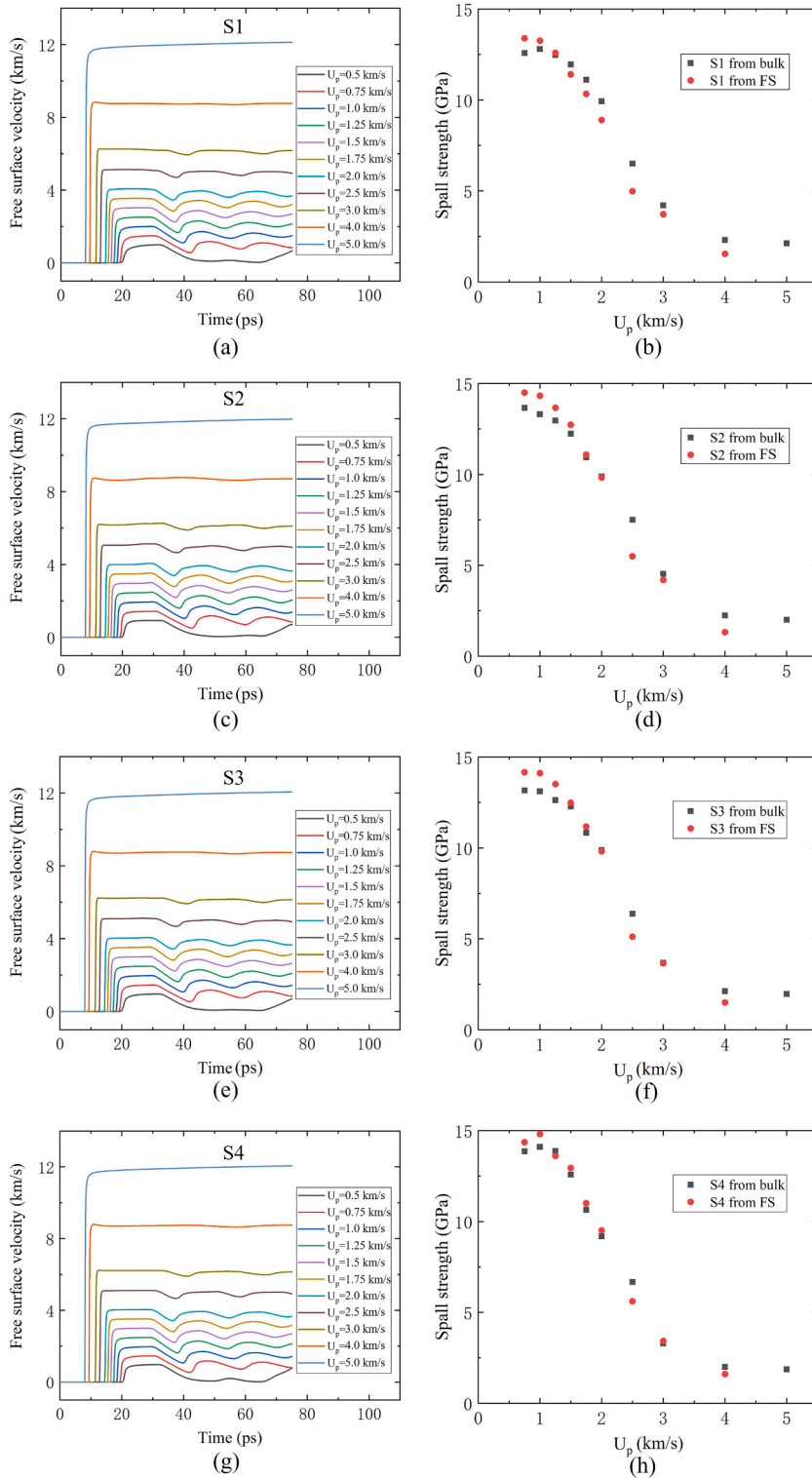
Fig. 15. FS velocity evolution of the shocked gradient and homogeneous samples under different particle velocities. (a) S1. (d) S2. (e) S3. (g) S4. The spall strengths, calculated from the bulk and FS, at different particle velocities are compared in (b) S1, (d) S2, (f) S3, and (h) S4, respectively.

directly from the spall region in bulk samples follow a similar trend with those calculated by the FS velocity in Eq. (13). As the shock strength increases, nanoglasses and MG naturally spall off at a faster rate, so the atomic velocity fluctuates strongly in the spall region. As a result, the initial defects are easier to nucleate in the spall region under strong shocks, which results in the spall strength decreases with increasing shock strength. Moreover, a higher temperature under strong shocks also weakens the spall strength to some extent. Finally, the comparison of spall strengths between the direct and indirect methods shows a good agreement in all samples because according to Eq. (14), the bulk sound speed used is reasonably changed with particle velocity. This illustrates that the spall strengths of the GNGs can be calculated with good results by the indirect method. However, there also are slight errors between the two methods because of the accuracy limited, i.e., the output frequency setup of MD simulations, the selection of probe sphere radius, and some factors ignored in the inherent assumptions of the spall analysis, etc.

Based on the above analysis, the spall strengths are also listed in Tables 2-5 for the S1, S2, S3, and S4 samples.

Fig. 16 displays the comparison of spall strengths between the S1 and S2 samples at different particle velocities. For the results of direct method (bulk), in the cases of $0.75 \leq U_p \leq 1.5$ km/s, the spall strengths of the S2 sample (positive gradient structure) are higher than those of the S1 sample (negative gradient structure). When the U_p exceeds 1.5 km/s, the spall strengths of the two samples tend to be the same. For the comparison of indirect method (FS), the spall strengths of the S2 sample are generally higher than those of the S1 sample. Therefore, the spall strengths in nanoglasses with the positive gradient structure are higher than those with the negative gradient structure.

In this work, the nucleation site of initial defects appears on the samples' right side under weak shocks, as shown in Fig. 14. Therefore, the grain size at the nucleation site in the S2 sample is larger than that in the S1 sample. In the previous uniaxial tensile simulations of $Cu_{64}Zr_{36}$ nanoglasses(Adibi et al., 2014), the strength of a sample with larger grain size is higher because the sparse distribution of grain interfaces leads to lower free volume. Thus, the lower free volume at the nucleation site in the S2 sample may cause a higher spall strength to some extent. Importantly, the gradient structures significantly affect temperature distribution, and the temperature during shock on the right side of the S2 sample is significantly lower than that of the S1 sample, as displayed in Fig. 10. In terms of shocked MGs, Wen et al.(Wen et al., 2019) pointed out that the spallation tends to occur in the high-temperature region rather than at the site associated with maximum tensile stress. The right side with a lower temperature in the S2 sample possesses a higher spall strength. As a result, the coupling effects of the lower free volume and temperature improve the spall strength of the S2 sample under weak shocks. However, as the U_p increases, the spall site gradually moves to left because the duration time of the shock pulse is constant, and the U_s increases with the U_p. Therefore, the spall site will have a higher temperature and smaller grain size in the S2 sample with the increase of U_p, so its spall strength decreases faster than the S1 sample.

In terms of the spall strengths, the S4 sample shows the highest value because it does not have glass-glass interfaces. Moreover, in the nanoglasses, the estimated spall strength is maximum in the S2 sample, at 14.49 GPa, followed by the S3 and S1 samples, at 14.16 and 13.39 GPa. Therefore, the usage of a positive gradient structure also further enhances the spall strength of homogeneous nanoglass. The difference in spall strengths between the S2 and S3 samples may be mainly caused by the temperature at the spall site rather than grain size. Under weak shocks, the difference in temperature between the S2 and S3 samples at the spall site is more significant than grain size. The positive gradient structure causes the shock wave to attenuate more energy on the left side of the sample, so the temperature of the S2 sample at the spall site (right side of sample) is higher than that of the S3 sample.

3.2.2. Defect evolution during spallation

To observe the defect evolution during spallation in detail, the slices with 1 nm thick, centered at 72 nm, along the Z-direction are selected in the S1 and S2 samples at $U_p = 0.75$ km/s. In Fig. 17, the slices in each row show the grain, stress, and temperature fields, respectively. The grain field indicates that the nucleation site of the initial void tends to be at the grain interfaces in nanoglasses. With further spallation, the initial void gradually grows, and the subsequent defects begin to nucleate. Interestingly, the subsequent defects also nucleate at the grain interfaces. Therefore, the defects of nanoglasses during spallation show heterogeneous nucleation at the grain interfaces, which is similar to conventional polycrystalline. These phenomena indicate that there is a difference in spall strengths

Table 2
Shock and spall parameters at different particle velocities along the negative gradient direction (S1). U_p is particle velocity; U_s is shock wave speed; C_b is bulk sound speed; Δu is pull-back velocity. σ_{sp}^I is spall strength from bulk GNG, while σ_{sp}^F is spall strength from FS velocity. The units for velocity and stress are km/s, GPa, respectively.

U_p	U_s	C_b	Δu	σ_{sp}^I	σ_{sp}^F
0.5	4.61	3.905	—	—	—
0.75	4.89	3.905	0.932	12.58	13.39
1.0	5.22	3.905	0.894	12.80	13.25
1.25	5.46	3.905	0.846	12.47	12.58
1.5	5.83	3.905	0.775	11.95	11.40
1.75	6.14	3.905	0.691	11.11	10.33
2.0	6.53	3.905	0.604	9.93	8.90
2.5	7.45	2.967	0.442	6.51	4.98
3.0	8.36	2.967	0.313	4.21	3.71
4.0	10.21	2.967	0.134	2.31	1.54
5.0	11.96	2.967	—	2.12	—

Table 3
Shock and spall parameters at different particle velocities along the positive gradient direction (S2). The units follow that of Table 2.

U_p	U_s	C_b	Δu	σ_{sp}^I	σ_{sp}^F
0.5	4.62	3.905	–	–	–
0.75	4.95	3.905	0.977	13.66	14.49
1.0	5.26	3.905	0.965	13.31	14.32
1.25	5.52	3.905	0.921	12.96	13.66
1.5	5.83	3.905	0.858	12.24	12.73
1.75	6.21	3.905	0.748	10.94	11.08
2.0	6.60	3.905	0.662	9.88	9.82
2.5	7.53	2.967	0.488	7.51	5.49
3.0	8.38	2.967	0.368	4.52	4.19
4.0	10.22	2.967	0.116	2.24	1.32
5.0	11.96	2.967	–	2.01	–

Table 4
Shock and spall parameters at different particle velocities in the homogeneous nanoglass (S3). The units follow that of Table 2.

U_p	U_s	C_b	Δu	σ_{sp}^I	σ_{sp}^F
0.5	4.61	3.905	–	–	–
0.75	4.93	3.905	0.962	13.16	14.16
1.0	5.23	3.905	0.959	13.11	14.11
1.25	5.51	3.905	0.918	12.63	13.51
1.5	5.81	3.905	0.848	12.28	12.48
1.75	6.24	3.905	0.759	10.84	11.17
2.0	6.53	3.905	0.666	9.88	9.81
2.5	7.55	2.967	0.467	6.38	5.11
3.0	8.32	2.967	0.326	3.68	3.65
4.0	10.19	2.967	0.134	2.12	1.50
5.0	11.93	2.967	–	1.97	–

Table 5
Shock and spall parameters at different particle velocities in the homogeneous $Cu_{64}Zr_{36}$ MG (S4). The units follow that of Table 2.

U_p	U_s	C_b	Δu	σ_{sp}^I	σ_{sp}^F
0.5	4.64	3.905	–	–	–
0.75	4.91	3.905	0.963	13.86	14.36
1.0	5.28	3.905	0.993	14.11	14.81
1.25	5.57	3.905	0.912	13.88	13.61
1.5	5.88	3.905	0.867	12.58	12.94
1.75	6.25	3.905	0.740	10.64	11.04
2.0	6.63	3.905	0.638	9.18	9.51
2.5	7.49	2.967	0.495	6.68	5.61
3.0	8.39	2.967	0.302	3.28	3.42
4.0	10.26	2.967	0.142	2.01	1.61
5.0	12.02	2.967	–	1.87	–

between the grain interiors and interfaces. The grain interfaces with a higher free volume have a lower strength during spallation. This further proves that in the GNGs, the grain size at the spall site does affect the spall strength. The stress field shows that as the voids nucleate and grow, large defects are formed in the sample, which leads to a decrease in tensile stress around the defects. However, the temperature around the defects displays a significant increase, as presented in the temperature field.

With a slight increase of shock strength, the heterogeneous nucleation of defects in nanoglasses disappears rapidly, as shown in Fig. 18. It is clear that the voids nucleate not only at the grain interfaces but also in the grain interiors. Moreover, the shock velocity of 1.25 km/s is not very high. These results indicate that during spallation, the nanoglasses do not exhibit a significant difference in strength between the grain interiors and interfaces, contrary to conventional polycrystalline. With the increasing U_p, the spall strengths in nanoglasses decrease, while the increase rate of tensile stress rises. As a result, the voids will nucleate simultaneously at both the grain interiors and interfaces if their strengths do not have a significant difference. Therefore, the strengths of the grain interiors and interfaces do have a difference during spallation, but the difference is not significant.

As we know, Yuan et al.(Yuan and Branicio, 2020) have proposed some possible methods to generate GNGs in experiments. For most experimentalists in the nanoglasses field, at present the experimental results can only give the mean-field sense information or sample states at some specific moments, which is not enough to reveal the details of atomic-scale mechanism. However, molecular dynamics can present the complete physical processes and calculate thermodynamic information in a micro and mesoscopic sample,
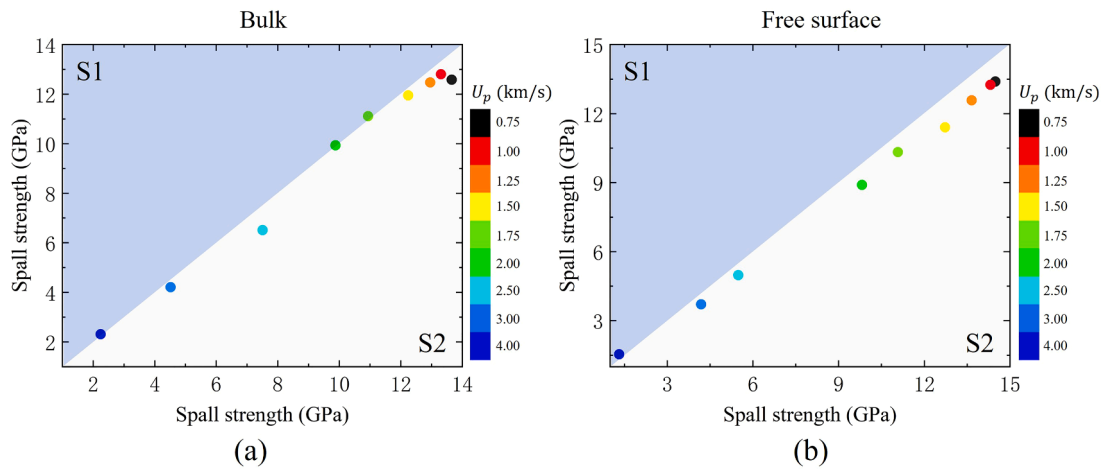
Fig. 16. The comparison of spall strengths between the S1 and S2 samples at different particle velocities. (a) Spall strengths obtained from bulk. (b) Spall strengths calculated by FS.
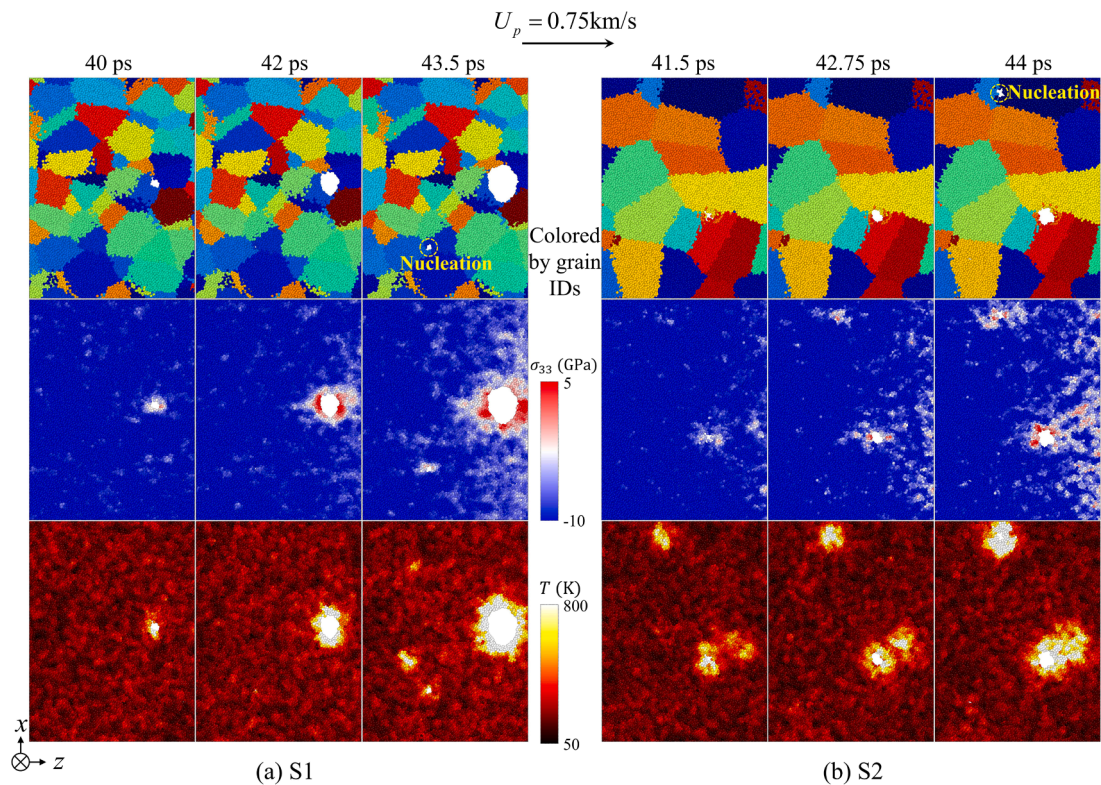

Fig. 17. The defect evolution during spallation for the GNGs at U_p = 0.75 km/s. (a) S1. (b) S2. There are three different analysis schemes used in the figures. The slices with 1 nm thick, centered at 72 nm, along the Z-direction are selected. The top row atoms are colored by grain IDs. Atoms in the second row are colored based on the shock stress. In the last row, the color of atoms represents the shock temperature. The sphere radius of the neighbor region used to average atomic physical quantities is 0.64 nm.

allowing experimentalists to get more idea about their works. We hope that the results of the current work and strategies on synthesis of GNGs will motivate experimental work in the nanoglasses field.

4. Conclusions

In present work, MD simulations are employed to study the shock characteristics and dynamic failure of $Cu_{64}Zr_{36}$ GNGs and
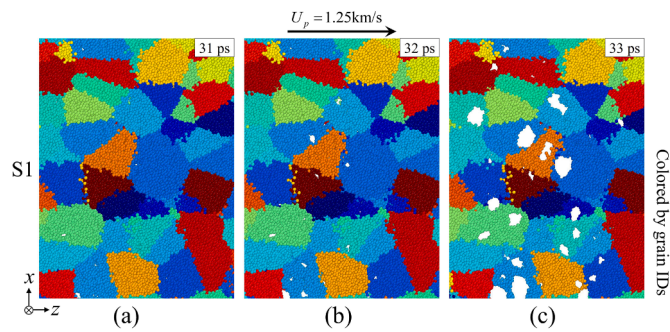
Fig. 18. The evolution of voids during spallation for the S1sample at $U_p = 1.25$ km/s. (a) 31 ps. (b) 32 ps. (c) 33 ps. A slice with 1 nm thick, centered at 64 nm, along the Z-direction is selected. The atoms are colored by grain IDs.

homogeneous samples in the particle velocity range of 0.5 to 5 km/s, where we analyzed the shear deformation behavior, shock stress, temperature, shock wave speed, spall fracture behavior, and spall strength. The simulations show that the number of mechanically stable <0,0,12,0> and <0,1,10,2> atomic clusters in grain interiors is higher than that in grain interfaces. Due to the relatively high APEs of these two types of clusters, the free volume in grain interfaces is larger than that in grain interiors. As a result, the region with a smaller grain size has a higher free volume. The higher free volume corresponds to a faster rate of shear deformation. Therefore, the shear deformation rate in the S1 sample gradually increases along the shock direction, whereas that in the S2 sample decreases. The difference in local shear strain rate has a significant impact on the shock wave profiles of stress, configurational entropy, and temperature. For the shock stress, the region with a smaller grain size presents lower value under weak shocks. This is because during shear deformation, a higher rate results in a greater relaxation of stress. However, as the shock strength increases, the time for shear deformation to reach a stable state gradually decreases, which means the difference in shear deformation rate is difficult to reflect in shock stress under strong shocks. Thus, the stress waveforms gradually become flat. For the configurational entropy, its value at the shock front depends strongly on the shear deformation rate. After the shock wave sweeps through, the shear deformation gradually stabilizes, so the effect of shear deformation rate will disappear. At this time, the configurational entropy is mainly determined by the degree of shear deformation (density of STZs). For the shock temperature, its increment is mainly determined by the degree of shear deformation. The degree of shear deformation in the local region during shock is controlled by the shear deformation rate and action time of shear stress. The shear deformation rate and action time are competitive in the S1 sample, whereas those are cooperative in the S2 sample. Therefore, the temperature waveforms along the shock direction progressively decrease at $U_p \leq 1.5$ km/s but increase at $U_p > 1.5$ km/s in the S1 sample, while those always gradually decrease in the S2 sample.

Importantly, there is a very weak dependence of the shock wave speed on grain size because of a similar chemically-disordered feature between the grain interiors and interfaces. This indicates a constant bulk sound speed in the GNGs. As a result, the indirect method, estimating spall strength, is still available for the GNGs. The spall strengths of the direct and indirect methods can match very well when applying the change in bulk sound speed at different particle velocities. In terms of the nanoglasses, the estimated spall strength is maximum in the S2 sample, at 14.49 GPa, followed by the S3 and S1 sample, at 14.16 and 13.39 GPa. The reason for the higher spall strength in the S2 sample is the positive gradient structure results in lower temperature and free volume in the spall region. For the spall evolution, the defects in nanoglasses show heterogeneous nucleation at the grain interfaces under a weaker shock ($U_p = 0.75$ km/s). However, with a slight increase of shock strength ($U_p = 1.25$ km/s), the heterogeneous nucleation of defects disappears rapidly. Therefore, the strengths of the grain interiors and interfaces do have a difference during spallation, but the difference is not significant.

Finally, a natural progression of this work is to analyze the heterogeneous nucleation of defects during shock. It is still unclear whether atomic composition, grain size, and initial temperature will affect the heterogeneous nucleation.

Data availability

All data used in this work can be regenerated based on the details provided in the Methodologies section.

CRediT authorship contribution statement

Yunlong Guan: Data curation, Software, Visualization, Writing – original draft, Writing – review & editing. **Weidong Song:** Funding acquisition, Methodology, Supervision, Writing – original draft, Writing – review & editing. **Yunjiang Wang:** Conceptualization, Funding acquisition, Resources, Validation, Writing – original draft, Writing – review & editing. **Shanshan Liu:** Data curation, Writing – review & editing. **Yongji Yu:** Data curation, Writing – review & editing.

Declaration of Competing Interest

The authors declare that they have no known competing financial interests or personal relationships that could have appeared to

influence the work reported in this paper.

Acknowledgement

References

Adibi, S., Branicio, P., Zhang, Y.-W., Joshi, S., 2014. Composition and grain size effects on the structural and mechanical properties of CuZr nanoglasses. Journal of Applied Physics 116, 043522.

Adjaoud, O., Albe, K., 2016. Interfaces and interphases in nanoglasses: Surface segregation effects and their implications on structural properties. Acta Materialia 113, 284–292.

Adjaoud, O., Albe, K., 2018. Microstructure formation of metallic nanoglasses: Insights from molecular dynamics simulations. Acta Materialia 145, 322–330.

Albe, K., Ritter, Y., Şopu, D., 2013. Enhancing the plasticity of metallic glasses: Shear band formation, nanocomposites and nanoglasses investigated by molecular dynamics simulations. Mechanics of Materials 67, 94–103.

Babanov, Y.A., Schvetsov, V.R., Sidorenko, A.F., 1995. Atomic structure of binary amorphous alloys by combined EXAFS and X-ray scattering. Physica B: Condensed Matter 208-209, 375–376.

Chen, C., Pei, T., Kuzmin, O., Zhang, Z., Ma, E., Th, J., Hosson, D., 2011. Intrinsic size effects in the mechanical response of taper-free nanopillars of metallic glass. Physical Review B 83, 180201.

H.S. Chen, Y. Waseda, 1979. Structure of glassy Zr(Cu and Nb)Ni alloys. physica status solidi (a) 51, 593-599.

Chen, S., Li, W.Q., Zhang, L., Fu, H.M., Li, Z.K., Zhu, Z.W., Li, H., Zhang, H.W., Wang, A.M., Wang, Y.D., Zhang, H.F., 2020. Dynamic compressive mechanical properties of the spiral tungsten wire reinforced Zr-based bulk metallic glass composites. Composites Part B: Engineering 199, 108219.

Cheng, Y., Sheng, H., Ma, E., 2008a. Relationship between structure, dynamics, and mechanical properties in metallic glass-forming alloys. Physical Review B 78.

Cheng, Y.Q., Cao, A.J., Ma, E., 2009. Correlation between the elastic modulus and the intrinsic plastic behavior of metallic glasses: The roles of atomic configuration and alloy composition. Acta Materialia 57, 3253–3267.

Cheng, Y.Q., Cao, A.J., Sheng, H.W., Ma, E., 2008b. Local order influences initiation of plastic flow in metallic glass: Effects of alloy composition and sample cooling history. Acta Materialia 56, 5263–5275.

Demaske, B.J., Phillpot, S.R., Spearot, D.E., 2018. Atomic-level deformation of CuxZr100-x metallic glasses under shock loading. Journal of Applied Physics 123, 215101.

Donovan, P.E., Stobbs, W.M., 1981. The structure of shear bands in metallic glasses. Acta Metallurgica 29, 1419–1436.

Eckert, J., Das, J., Pauly, S., Duhamel, C., 2007. Mechanical properties of bulk metallic glasses and composites. Journal of Materials Research 32, 635–638.

Falk, M.L., Langer, J.S., 1998. Dynamics of viscoplastic deformation in amorphous solids. Physical Review E 57, 7192–7205.

Falk, M.L., Langer, J.S., 2011. Deformation and Failure of Amorphous. Solidlike Materials. Annual Review of Condensed Matter Physics 2, 353–373.

Fang, J.X., Vainio, U., Puff, W., Würschum, R., Wang, X.L., Wang, D., Ghafari, M., Jiang, F., Sun, J., Hahn, H., Gleiter, H., 2012. Atomic structure and structural stability of Sc75Fe25 nanoglasses. Nano Lett 12, 458–463.

Feng, S., Qi, L., Wang, L., Pan, S., Ma, M., Zhang, X., Li, G., Liu, R., 2015. Atomic structure of shear bands in Cu64Zr36 metallic glasses studied by molecular dynamics simulations. Acta Materialia 95, 236–243.

Feng, S., Zhao, W., Jiao, W., Yu, P., Li, G., Qi, L., Liu, R., 2014. Effect of Voronoi volume on fluctuation at initial deformation of amorphous alloys. Journal of Applied Physics 116, 133520.

Feng, S.D., Qi, L., Wang, L.M., Yu, P.F., Zhang, S.L., Ma, M.Z., Zhang, X.Y., Jing, Q., Ngai, K.L., Greer, A.L., Li, G., Liu, R.P., 2016. Structural feature of Cu64Zr36 metallic glass on nanoscale: Densely-packed clusters with loosely-packed surroundings. Scripta Materialia 115, 57–61.

Fu, X.L., Li, Y., Schuh, C.A., 2007. Temperature, strain rate and reinforcement volume fraction dependence of plastic deformation in metallic glass matrix composites. Acta Materialia 55, 3059–3071.

Gan, K.F., Jiang, S.S., Huang, Y.J., Yin, H.B.C., Sun, J.F., Ngan, A.H.W., 2019. Elucidating how correlated operation of shear transformation zones leads to shear localization and fracture in metallic glasses: Tensile tests on CuZr based metallic-glass microwires, molecular dynamics simulations, and modelling. International Journal of Plasticity 119, 1–20.

Greer, A., Cheng, Y.Q., Ma, E., 2013. Shear bands in metallic glasses. Materials Science and Engineering: R: Reports 74, 71–132.

Guan, Y.-L., Dai, L.-S., Shao, J.-L., Song, W.-D., 2021. Molecular dynamics study on the nanovoid collapse and local deformation in shocked Cu50Zr50 metallic glasses. Journal of Non-Crystalline Solids 559, 120703.

Hahn, E.N., Germann, T.C., Ravelo, R., Hammerberg, J.E., Meyers, M.A., 2017. On the ultimate tensile strength of tantalum. Acta Materialia 126, 313–328.

Hamel, S., Benedict, L.X., Celliers, P.M., Barrios, M.A., Boehly, T.R., Collins, G.W., Döppner, T., Eggert, J.H., Farley, D.R., Hicks, D.G., Kline, J.L., Lazicki, A., LePape, S., Mackinnon, A.J., Moody, J.D., Robey, H.F., Schwegler, E., Sterne, P.A., 2012. Equation of state of CH1.36: First-principles molecular dynamics simulations and shock-and-release wave speed measurements. Physical Review B 86, 094113.

Hammond, K.D., 2020. Parallel point defect identification in molecular dynamics simulations without post-processing: A compute and dump style for LAMMPS. Computer Physics Communications 247, 106862.

He, G., Eckert, J., Löser, W., Schultz, L., 2003. Novel Ti-base nanostructure–dendrite composite with enhanced plasticity. Nature Materials 2, 33–37.

Huang, X., Ling, Z., Dai, L.H., 2014. Ductile-to-brittle transition in spallation of metallic glasses. Journal of Applied Physics 116, 143503.

Inoue, A., Wada, T., Louzguine-Luzgin, D.V., 2007. Improved mechanical properties of bulk glassy alloys containing spherical pores. Materials Science and Engineering: A 471, 144–150.

Islam, M., Thakur, M.S.H., Mojumder, S., Al Amin, A., Islam, M.M., 2020. Mechanical and vibrational characteristics of functionally graded Cu–Ni nanowire: A molecular dynamics study. Composites Part B: Engineering 198, 108212.

Jian, W.R., Yao, X.H., Wang, L., Tang, X.C., Luo, S.N., 2015. Short- and medium-range orders in Cu46Zr54 metallic glasses under shock compression. Journal of Applied Physics 118, 015901.

Kim, Y.M., Lee, B.J., 2008. A modified embedded-atom method interatomic potential for the Cu-Zr system. Journal of Materials Research 23, 1095–1104.

Klement, W., Willens, R.H., Duwez, P.O.L., 1960. Non-crystalline Structure in Solidified Gold–Silicon Alloys. Nature 187, 869–870.

Kosiba, K., Şopu, D., Scudino, S., Zhang, L., Bednarcik, J., Pauly, S., 2019. Modulating heterogeneity and plasticity in bulk metallic glasses: Role of interfaces on shear banding. International Journal of Plasticity 119, 156–170.

Laridjani, M., Sadoc, J.F., 1988. Amorphous CuZr2 partial distribution functions using the anomalous diffraction technique. Journal of Non-Crystalline Solids 106, 42–46.

Lewandowski, J., 2001. Bulk Metallic Glasses. III. Effects of Annealing and Changes in Stress State on Fracture Toughness of Bulk Metallic Glass. Materials Transactions 42, 633–637.

Li, W., Hahn, E.N., Yao, X., Germann, T.C., Feng, B., Zhang, X., 2020. On the grain size dependence of shock responses in nanocrystalline sic ceramics at high strain rates. Acta Materialia 200, 632–651.

Li, W., Hahn, E.N., Yao, X., Germann, T.C., Zhang, X., 2019. Shock induced damage and fracture in SiC at elevated temperature and high strain rate. Acta Materialia 167, 51–70.

Liu, H., Hao, M., Tao, M., Sun, Y., Xie, W., 2019. Molecular dynamics simulation of dislocation evolution and surface mechanical properties on polycrystalline copper. Applied Physics A 125, 214.

Luo, Y., Yang, G., Shao, Y., Yao, K., 2018. The effect of void defects on the shear band nucleation of metallic glasses. Intermetallics 94, 114–118.

Ma, C., Wang, G.-X., Ye, C., Dong, Y., 2017. Shocking of metallic glass to induce microstructure heterogeneity: A molecular dynamics study. Journal of Applied Physics 122, 095102.

Mattern, N., Schöps, A., Kühn, U., Acker, J., Khvostikova, O., Eckert, J., 2008. Structural behavior of CuxZr100−x metallic glass (x=35−70). Journal of Non-Crystalline Solids 354, 1054–1060.

Mauro, N., Wessels, V., Bendert, J., Klein, S., Gangopadhyay, A., Kramer, M., Hao, S., Rustan, G., Kreyssig, A., Goldman, A., Kelton, K., 2011. Short- and medium-range order in Zr80Pt20 liquids. Physical Review B 83, 1841091–1841098.

Mendelev, M.I., Kramer, M.J., Ott, R.T., Sordelet, D.J., Yagodin, D., Popel, P., 2009. Development of suitable interatomic potentials for simulation of liquid and amorphous Cu–Zr alloys. Philosophical Magazine 89, 967–987.

Mendelev, M.I., Sun, Y., Zhang, F., Wang, C.Z., Ho, K.M., 2019. Development of a semi-empirical potential suitable for molecular dynamics simulation of vitrification in Cu-Zr alloys. The Journal of Chemical Physics 151, 214502.

Narayan, R.L., Tandaiya, P., Narasimhan, R., Ramamurty, U., 2014. Wallner lines, crack velocity and mechanisms of crack nucleation and growth in a brittle bulk metallic glass. Acta Materialia 80, 407–420.

Pǎduraru, A., Kenoufi, A., Bailey, N.P., Schiøtz, J., 2007. An Interatomic Potential for Studying CuZr Bulk Metallic Glasses. Advanced Engineering Materials 9, 505–508.

Pan, S., Feng, S., Qiao, J., Wang, W., Qin, J., 2015. Correlation between local structure and dynamic heterogeneity in a metallic glass-forming liquid. Journal of Alloys and Compounds 664.

Pauly, S., Gorantla, S., Wang, G., Kühn, U., Eckert, J., 2010. Transformation-mediated ductility in CuZr-based bulk metallic glasses. Nature Materials 9, 473–477.

Piaggi, P.M., Parrinello, M., 2017. Entropy based fingerprint for local crystalline order. The Journal of Chemical Physics 147, 114112.

Polk, D.E., Turnbull, D., 1972. Flow of melt and glass forms of metallic alloys. Acta Metallurgica 20, 493–498.

Qiu, C., Su, Y., Yang, J., Wang, X., Chen, B., Ouyang, Q., Zhang, D., 2021. Microstructural characteristics and mechanical behavior of SiC(CNT)/Al multiphase interfacial micro-zones via molecular dynamics simulations. Composites Part B: Engineering 220, 108996.

Ramamurty, U., Lee, M.L., Basu, J., Li, Y., 2002. Embrittlement of a bulk metallic glass due to low-temperature annealing. Scripta Materialia 47, 107–111.

Ritter, Y., Şopu, D., Gleiter, H., Albe, K., 2011. Structure, stability and mechanical properties of internal interfaces in Cu64Zr36 nanoglasses studied by MD simulations. Acta Materialia 59, 6588–6593.

Schuh, C.A., Hufnagel, T.C., Ramamurty, U., 2007. Mechanical behavior of amorphous alloys. Acta Materialia 55, 4067–4109.

Sha, Z.-D., Branicio, P.S., Lee, H.P., Tay, T.E., 2017. Strong and ductile nanolaminate composites combining metallic glasses and nanoglasses. International Journal of Plasticity 90, 231–241.

Sha, Z.D., Branicio, P.S., Pei, Q.X., Liu, Z.S., Lee, H.P., Tay, T.E., Wang, T.J., 2015. Strong and superplastic nanoglass. Nanoscale 7, 17404–17409.

Shan, Z.-W., Li, J., Cheng, Y., Minor, A., Asif, S., Warren, O., Ma, E., 2008. Plastic flow and failure resistance of metallic glass: Insight from in situ compression of nanopillars. Physical Review B 77.

Shao, J.-L., He, A.-M., Wang, P., 2018. Atomistic simulations on the dynamic properties of shock and release melting in single crystal Al. Computational Materials Science 151, 240–245.

Sharma, P., Yubuta, K., Kimura, H., Inoue, A., 2009. Brittle metallic glass deforms plastically at room temperature in glassy multilayers. Physical Review B 80.

Shi, Y., Falk, M., 2006. Atomic-scale simulations of strain localization in three-dimensional model amorphous solids. Physical Review B 73.

Shimizu, F., Ogata, S., Li, J., 2007. Theory of Shear Banding in Metallic Glasses and Molecular Dynamics Calculations. Materials Transactions 48, 2923–2927.

Şopu, D., Ritter, Y., Gleiter, H., Albe, K., 2011. Deformation behavior of bulk and nanostructured metallic glasses studied via molecular dynamics simulations. Physical Review B 83.

Spaepen, F., 1977. A microscopic mechanism for steady state inhomogeneous flow in metallic glasses. Acta Metallurgica 25, 407–415.

Stukowski, A., 2014. Computational Analysis Methods in Atomistic Modeling of Crystals. JOM 66, 399–407.

Tang, X.C., Li, C., Li, H.Y., Xiao, X.H., Lu, L., Yao, S.N., 2019. Cup-cone structure in spallation of bulk metallic glasses. Acta Materialia 178, 219–227.

Tang, X.C., Yao, X.H., Wilkerson, J.W., 2021. A micromechanics-based framework to predict transitions between dimple and cup-cone fracture modes in shocked metallic glasses. International Journal of Plasticity 137, 102884.

Turnbull, D., Cohen, M., 1961. Free-Volume Model of the Amorphous Phase: Glass Transition. The Journal of Chemical Physics 34, 120–125.

Wada, T., Inoue, A., Greer, A.L., 2005. Enhancement of room-temperature plasticity in a bulk metallic glass by finely dispersed porosity. Applied Physics Letters 86, 251907.

Wang, C., Guo, X., Ivanisenko, Y., Goel, S., Nirschl, H., Gleiter, H., Hahn, H., 2017. Atomic structure of Fe90Sc10 glassy nanoparticles and nanoglasses. Scripta Materialia 139, 9–12.

Wang, J., Li, R., Hua, N., Zhang, T., 2011. Co-based ternary bulk metallic glasses with ultrahigh strength and plasticity. Journal of Materials Research 26, 2072–2079.

Wang, S., Wang, C., Li, M., Huang, L., Ott, R., Kramer, M., Sordelet, D., Ho, K., 2008. Short and medium-range order in a Zr73Pt27 glass: Experimental and simulation studies. Physical Review B 78.

Way, C., Shaw, T., Wadhwa, P., Busch, R., 2007. Shear rate dependence of viscosity and configurational entropy of the Zr41.2Ti13.8Cu12.5Ni10.0Be22.5 metallic glass forming liquid. Journal of Alloys and Compounds 434-435, 88–91.

Wei, Z., Xu, X., 2021. Gradient design of bio-inspired nacre-like composites for improved impact resistance. Composites Part B: Engineering 215, 108830.

Weissmüller, J., Birringer, R., Gleiter, H., 1992. Nanostructured Crystalline and Amorphous Solids. Key Engineering Materials 77-78, 161–170.

Wen, P., Demaske, B., Phillpot, S., Spearot, D., 2019. Void collapse and subsequent spallation in Cu50Zr50 metallic glass under shock loading by molecular dynamics simulations. Journal of Applied Physics 125, 215903.

Wen, P., Demaske, B., Spearot, D.E., Phillpot, S.R., 2018. Shock compression of CuxZr100−xmetallic glasses from molecular dynamics simulations. Journal of Materials Science 53, 5719–5732.

Winkler, B., Friedrich, A., Wilson, D.J., Haussühl, E., Krisch, M., Bosak, A., Refson, K., Milman, V., 2008. Dispersion Relation of an OH-Stretching Vibration from Inelastic X-Ray Scattering. Physical Review Letters 101, 065501.

Wu, F.F., Zheng, W., Wu, S.D., Zhang, Z.F., Shen, J., 2011. Shear stability of metallic glasses. International Journal of Plasticity 27, 560–575.

Xi, F., Yu, Y., Dai, C., Zhang, Y., Cai, L., 2010. Shock compression response of a Zr-based bulk metallic glass up to 110 GPa. Journal of Applied Physics 108, 083537.

Yang, L., Guo, G.Q., Chen, L.Y., Huang, C.L., Ge, T., Chen, D., Liaw, P.K., Saksl, K., Ren, Y., Zeng, Q.S., LaQua, B., Chen, F.G., Jiang, J.Z., 2012. Atomic-Scale Mechanisms of the Glass-Forming Ability in Metallic Glasses. Physical Review Letters 109, 105502.

Yuan, S., Branicio, P.S., 2020. Gradient microstructure induced shear band constraint, delocalization, and delayed failure in CuZr nanoglasses. International Journal of Plasticity 134, 102845.

Zhao, P., Li, J., Wang, Y., 2013. Heterogeneously randomized STZ model of metallic glasses: Softening and extreme value statistics during deformation. International Journal of Plasticity 40, 1–22.